Ultrasonic Imaging of the Onset and Growth of Fractures within Partially Saturated Whitby Mudstone using Coda-Wave Decorrelation Inversion

Reuben Zotz-wilson[1,1], Lisanne ANR Douma[2,2], Joel Sarout[3,3], Jeremie Dautriat[4,4], David N. Dewhurst[4,4], and Auke Barnhoorn[1,1]

[1]Delft University of Technology
[2]TU Delft
[3]CSIRO Energy
[4]Commonwealth Scientific and Industrial Research Organisation (CSIRO)

November 30, 2022

Abstract

Using active ultrasonic source survey data, Coda-wave Decorrelation (CWD) time-lapse imaging during the triaxial compression of Whitby Mudstone cores provides a 3-D description of the evolution and redistribution of inelastic strain concentrations. Acoustic Emissions (AEs) monitoring is also performed between any two consecutive surveys. From these data, we investigate the impact of initial water saturation S_w on the onset, growth, and reactivation of inelastic deformation, compared to the post-deformation fracture network extracted from X-ray tomography scans. Our results indicate for the applied strain-rate and degree of initial water saturation, and within the frequency range of our ultrasonic transducers (0.1 to 1 MHz), that inelastic strain localisation and propagation in the Whitby Mudstone does not radiate AEs of sufficient magnitude to be detected above the average noise level. This is true for both the initial onset of inelasticity (strain localisation), and during macroscopic failure. In contrast, the CWD results indicate the onset of what is interpreted as localised regions of inelastic strain at less than fifty percent of the peak differential stress the Whitby Mudstone can sustain. The seemingly aseismic nature of these clay-rich rocks suggests the gradual development of inelastic strain, from the microscopic diffuse damage, up until the macroscopic shear failure.

Ultrasonic Imaging of the Onset and Growth of Fractures within Partially Saturated Whitby Mudstone using Coda-Wave Decorrelation Inversion

Reuben Zotz-Wilson[1], **Lisanne A.N.R. Douma**[1], **Joel Sarout**[2], **Jeremie Dautriat** [2], **David Dewhurst** [2], **Auke Barnhoorn**[1]

[1]Delft University of Technology, Faculty of Civil Engineering and Geoscience. Stevinweg 1, 2628 CN Delft, The Netherlands

[2]CSIRO - Energy, Perth Australia.

Key Points:

- Inversion of Coda-Wave Decorrelation data allows the imaging of sub-wavelength strain localization.
- CWD inversion is capable of imaging aseismic triaxial deformation and failure of the Whitby mudstone.
- Onset of aseismic sub-wavelength precursory strain imaged at less than 50% of peak differential stress.

Corresponding author: Reuben Zotz-Wilson, rdzotz@gmail.com

Abstract

Using active ultrasonic source survey data, Coda-wave Decorrelation (CWD) time-lapse imaging during the triaxial compression of Whitby Mudstone cores provides a 3-D description of the evolution and redistribution of inelastic strain concentrations. Acoustic Emissions (AEs) monitoring is also performed between any two consecutive surveys. From these data, we investigate the impact of initial water saturation S_w on the onset, growth, and reactivation of inelastic deformation, compared to the post-deformation fracture network extracted from X-ray tomography scans. Our results indicate for the applied strain-rate and degree of initial water saturation, and within the frequency range of our ultrasonic transducers (0.1 to 1 MHz), that inelastic strain localisation and propagation in the Whitby Mudstone does not radiate AEs of sufficient magnitude to be detected above the average noise level. This is true for both the initial onset of inelasticity (strain localisation), and during macroscopic failure. In contrast, the CWD results indicate the onset of what is interpreted as localised regions of inelastic strain at less than fifty percent of the peak differential stress the Whitby Mudstone can sustain. The seemingly aseismic nature of these clay-rich rocks suggests the gradual development of inelastic strain, from the microscopic diffuse damage, up until the macroscopic shear failure.

1 Introduction

Mudstones play an important role in many civil infrastructure, energy and resource projects globally. They act as impermeable seals in conventional hydrocarbon or carbon capture reservoirs [*Busch et al.*, 2008; *Armitage et al.*, 2016], or as both a source [*Jianghui et al.*, 2012] and reservoir rock [*Aplin and Macquaker*, 2011] in unconventional hydrocarbon projects. Several permanent nuclear storage projects plan to [*Brookins*, 1976; *Vomvoris et al.*, 2013] or already employ [*Aikas and Sundell*, 2014] mudstones as the host rock for both high and low grade radioactive waste. Due to their global abundance [*Garrels and Mackenzie*, 1969], civil infrastructure project such as tunnels, dams, and bridges often directly interact with mudstones [*Yoshida et al.*, 1997; *Wang et al.*, 2013; *Izumi et al.*, 1998], presenting a variety of engineering challenges. Furthermore, shales and mudstones are considered as a key input when developing susceptibility maps for environmental damage due to landslides [*Ayalew and Yamagishi*, 2005]. It is therefore essential to gain an understanding of the mechanical properties of mudstones under a variety of environmental conditions. To this end, laboratory triaxial testing of core samples subjected to realistic

subsurface temperature, pressure, stress, and saturation conditions are essential. While the bulk core properties are generally attainable by measurements at the boundary, the determination of the time and location at which inelastic changes develop, requires techniques which are sensitive to localised changes within the core. Acoustic Emissions (AEs) monitoring has been a commonly applied technique within rock-mechanics laboratories for more than two decades [*Lockner*, 1993; *Lei et al.*, 2004; *Heap et al.*, 2009; *Sarout et al.*, 2017], enabling the rate, location, and effective stress at which fracturing develops to be extracted from passive acoustic monitoring. Some inherent limitation of AE monitoring are that it requires: (i) the magnitude of acoustic energy emitted during fracturing to be sufficiently large, and (ii) within the dynamic range that it is detectable by the available sensor network. Further, AE monitoring is unable to detect inelastic changes which are truly aseismic in nature [*Main*, 1990].

In this study, we apply both active source acoustic and passive AE monitoring, on three laboratory scale core samples of different initial water saturation. The aim is to monitor both the location and time of fracturing from active source monitoring, in comparison with the onset of AE, thereby providing an indication of the degree to which pre-seismic changes occur. This is based on the premise that active source methods do not rely on the spontaneous emission of acoustic energy in order to detect the presence of inelastic deformation, and therefore remain, in principle, sensitive to aseismic fracturing. While there have been a number of velocity tomography monitoring applications in laboratory rock deformation experiments [*Jansen et al.*, 1993; *Brantut*, 2018; *Aben et al.*, 2019], enabling the three-dimensional imaging of rock fracturing, in this work we apply Coda-Wave Decorrelation (CWD) inversion for the first time within experimental rock mechanics. The CWD method makes use of the coda of recorded waveforms and therefore can be expected to display improved sensitivity when compared to methods which rely on the coherent arrivals [*Snieder*, 2002; *Grêt*, 2005; *Zotz-Wilson et al.*, 2019]. While the first publication and experimental application of CWD demonstrates the ability of the method to locate, in a probabilistic sense, the formation of a single defect within a concrete slab [*Larose et al.*, 2010], in this study we apply a least-squares approach which has the potential to locate, in terms of a physical quantity, multiple regions of change simultaneously [*Planès et al.*, 2015].

The results of this study, monitoring the active and passive acoustic response of mudstone samples of differing initial water saturation, provides valuable information on

the development of both microscopic inelastic strain (diffuse damage) and the emergence of larger coalesced macroscopic shear fractures.

2 Materials and Methods

2.1 Sample material and preparation

The mudstone samples originate from the outcropping Whitby Mudstone formation (WMF), United Kingdom (UK). The WMF is deposited in the East-English Cleveland Basin in anoxic bottom conditions [*Powell*, 2010]. This Toarcian Age mudstone formation consists of three members, including the Grey Shale Member, Mulgrave Shale Member, and Alum Shale Member [*Powell*, 2010]. The Mulgrave Shale Member (Lower Jurassic) is the lateral equivalent of the Dutch Posidonia Shale Formation (PSF), the main shale gas target in the Netherlands. The maximum burial depth of the mudstones in the Cleveland Basin is ~4 km, where top of the Lower Jurassic does not exceed ~2.5 km [*Pye*, 1985]. The WMF has been considered an analogue for the Dutch PSF [*Zijp et al.*, 2015], since the PSF is not outcropping in the Netherlands, core material is badly preserved, and available log data is limited.

The WMF is a relatively clay-rich rock, composed of 50 % to 70 % inter-layered illite/smectite, illite, and kaolinite [*Houben et al.*, 2016a]. The organic matter (TOC ~6 %) is often inter-layered within the matrix [*Zijp et al.*, 2015; *Houben et al.*, 2016a]. The porosity of the mudstones originating from the Mulgrave Shale Member is ~13 %, based on the wet and dry mass of a mudstone core [*Douma et al.*, 2019]. The matrix permeability is in the range of $10 \times 10^{-23}\,\mathrm{m}^2$ to $10 \times 10^{-18}\,\mathrm{m}^2$, and pore diameters are between 72 and 300 nm [*Houben et al.*, 2016b].

Mudstone blocks are sampled from a wave-cut platform on the east coast of England, north of Whitby (UK), near Runswick Bay. The mudstones in the outcrop are submerged daily by seawater, due to the tidal cycle. Immediately after sampling, the mudstone blocks were stored in seawater to prevent initial pore water loss. Seawater was used because the assumption was made that the pore fluid of the mudstones became in chemical equilibrium with the seawater over geological time. Cylindrical core plugs were cored normal to the bedding out of the same larger sample block and have a length of ~80 mm and a diameter of ~40 mm . During coring, seawater was used as cooling fluid to prevent shrinkage or swelling of the clays. After coring, the core plugs were stored at room

temperature in three different desiccators with a constant relative humidity atmosphere of ~85 %, 75 %, and 35 %. At these relative humidities, the corresponding water saturations achieved after several weeks (until mass stabilization) are ~70 ± 10 %, ~58 ± 10 %, and ~28 ± 10 %, obtained by subtracting the brine volume divided by the pore volume from the initial water saturation [*Douma et al.*, 2019]. The different relative humidity atmospheres were created by using oversaturated brine solutions, as explained in detail by *Laloui et al.* [2013]. The three core plugs were used for rock mechanical testing after equilibrating for approximately two months in a desiccator.

2.2 Experimental Procedure

The experimental setup used for the mechanical and ultrasonic testing includes a triaxial stress vessel, multichannel ultrasonic monitoring system, and ultrasonic P-wave transducers. A similar setup was used by *Sarout et al.* [2015, 2017] and *Douma et al.* [2019]. The partially-saturated core plugs are placed in a Viton sleeve to prevent contact with the surrounding confining oil. Two opposed linear variable differential transformers (LVDTs) monitor the axial displacement. The local circumferential strain is measured with a strain gauge-based cantilever mounted through the Viton sleeve, directly on the lateral surface of the core plug.

Two aluminium spacers (38 mm diameter; 1 mm thickness) are placed on top and bottom of the partially-saturated core plugs (see fig. 1), to achieve macroscopically undrained conditions during the deformation of the rock. This means that there is no pore pressure control or monitoring during testing, and that no fluid is allowed to exit the core plug. The experiments are all performed at room temperature (22.0 ± 1.5 °C). A detailed description of the experimental procedure is given by *Douma et al.* [2019], though in essence this can be summarised as:

- An increase in confining pressure at a rate of 0.5 MPa min^{-1} up to 15 MPa, followed by a consolidation stage of about three days under isotropic stress conditions.
- Subsequently, a vertical stress was applied orthogonal to the bedding with a constant axial strain rate of 1×10^{-7} s^{-1} until failure of the WMF sample.

A total of fourteen piezo-ceramic-based P-wave transducers (footprint diameter 6 mm, dominant resonant frequency 0.5 MHz) are directly attached to the Whitby Mudstone

(WM) sample (see fig. 1), through the Viton sleeve, which record the ultrasonic signals propagated through the sample from a particular transducer. Each transducer acts sequentially as a source S_i, while the other thirteen transducers act as receivers R_j. During each survey, multiple repeat measurements are performed, and the recorded waveforms are stacking at each R_j, thereby improving the Signal-to-Noise Ratio (SNR). Each survey consists of 182 (14×13) stacked waveforms, recorded during a time window of 410 µs, at a sampling rate of 10 MHz, and an amplitude resolution of 12-bit [*Sarout et al.*, 2015]. Surveys are conducted at regular time intervals of either 2.5 or 5 min during a deformation experiment. Each active source survey takes ~30 s, in the time between all fourteen transducers are switched to passive monitoring mode, allowing the detection and recording of spontaneous fracturing events referred to as Acoustic Emissions (AEs). In preparation for subsequent processing, the data recorded during each survey p are arranged into an impulse response data cube $\mathbf{D}_p$, with each waveform stored corresponding to S_i in rows, R_j in columns, for P surveys.

In order to ascertain the actual extent of the fracture network formed during triaxial failure, all tested WM samples were scanned before and after experimentation using an X-ray computed tomography scanner. The created data set has a voxel size of 100 x 100 x 400 μm.

2.3 Coda-Wave Decorrelation Inversion Procedure

This section summaries the theory and inversion workflow applied to the three impulse response data cubes $\mathbf{D}_n$ obtained from the three triaxial experiments. The work by *Larose et al.* [2010] was the first description of what we refer to as Coda-Wave Decorrelation Inversion, in which the formation of a single defect within a concrete block was located by active source time-lapse measurements from several ultrasonic receivers. Since this initial publication, other works have applied CWD inversion to monitor the formation of cracks in concrete structures [*Larose et al.*, 2015; *Zhang et al.*, 2016], or study changes due to volcanic [*Obermann et al.*, 2013] or tectonic [*Obermann et al.*, 2014, 2019] activity. In this work, we apply a linear least squares inversion method, for the time-lapse monitoring of shale deformation and failure under triaxial stress conditions. The python code developed by *Zotz-Wilson* [2019] is used for this purpose. For a detailed description of the theory employed, the reader is referred to *Planès et al.* [2015].

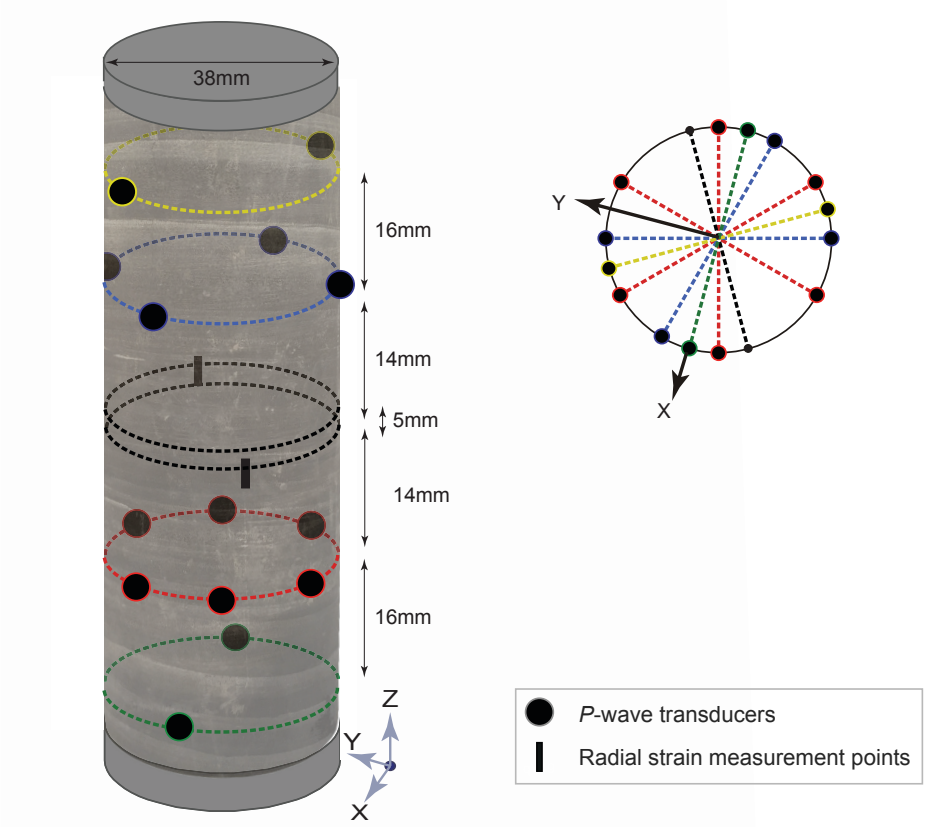

Figure 1. Configuration 14 radially mounted transducers, aligned with the middle of each core sample, after *Sarout et al.* [2015, 2017]; *Douma et al.* [2019].

The basic premise of CWD is that a change in the scattering properties of a medium, can be inferred by a comparison between wavefields recorded before and after the change. This comparison is performed via a normalised cross-correlation, with the measured decorrelation coefficient K^m calculated for a time window $[t_k - t_w, t_k + t_w]$ within the coda. Similar to Coda-Wave Interferometry (CWI) which relates the phase shift of this correlation to a change in elastic wavespeed [*Larose and Hall*, 2009; *Payan et al.*, 2009; *Zhang et al.*, 2012; *Grêt et al.*, 2006] or temperature [*Grêt et al.*, 2006; *Weaver and Lobkis*, 2000; *Larose et al.*, 2006] of the medium, CWD relates the corresponding K^m to a change in the scattering properties of the medium. In terms of data processing, for each survey p, the measured decorrelation coefficient K^m_{ij} between a reference survey D_{ref} and survey D_p obtained after perturbation, is calculated for each source i and receiver j and non-overlapping window of width $2t_w$ within the coda. The resulting data decorrelation matrix

$\mathbf{K}_p^m$ of dimensions $[S_i, R_j, t_k]$ for each survey p, serves as the observed data input to an inversion scheme.

In order to relate each K_{ij}^m for various windows within the coda to localised change within the core sample, a theoretical estimation of the decorrelation coefficient K_{ij}^m [*Rossetto et al.*, 2011], associated with a change in scattering at location $\mathbf{r}$ is calculated as ,

$$K_{ij}^T(\mathbf{r}, t_k) = \frac{V_0 \sigma_T}{2} Q(S_i, R_j, \mathbf{r}, t_k), \tag{1}$$

where σ_T is the scattering cross-section of a defect at position $\mathbf{r}$ within a medium with a background velocity V_0. The sensitivity kernel $Q(...)$ used in this work was derived by *Rossetto et al.* [2011] as,

$$Q(S_i, R_j, \mathbf{r}, t_k) = \frac{1}{4\pi\mathcal{D}} \left(\frac{1}{s_i} + \frac{1}{r_j} \right) \exp \left[\frac{||S_i - R_j||^2 - (s_i + r_j)^2}{4\mathcal{D}t_k} \right], \tag{2}$$

where $s_i = ||S_i - \mathbf{r}||$, $r_j = ||R_j - \mathbf{r}||$ and $\mathcal{D}$ is the diffusivity of the wavefield within the medium. This kernel quantifies the expected sensitivity of a particular sensor arrangement (S_i, R_j,) at elapse time t_k to a perturbation at position $\mathbf{r}$. For the three-dimensional visualisation of each sensitivity kernel between different S_i - R_j pairs, see S1. The core volume is then discretised into tetrahedra, allowing eq. (1) to be calculated at the centre of each. A forward problem is then formulated in vector/matrix form as,

$$\mathbf{K}_p^m = \mathbf{G}\mathbf{m}, \tag{3}$$

where $\mathbf{K}_p^m$ is arranged into a vector of measured decorrelation coefficients at survey p, for each S_i - R_j pair, and correlation window. The matrix $\mathbf{G}$ stores the sensitivity kernels $Q(S_i, R_j, \mathbf{r}, t_k)$ row-wise, calculated at each tetrahedron. The true model parameters $\mathbf{m}$ is a vector containing the density of σ_T perturbations within each tetrahedron given as σ_{T_ρ} with the dimensions $\mathrm{mm}^2/\mathrm{mm}^3$. A least-squares formulation is adopted [*Tarantola*, 2005], in order to invert for the model parameters $\tilde{\mathbf{m}}$. As σ_{T_ρ} must be positive, an iterative procedure is applied for each $\mathbf{K}_p^m$ by which any negative $\tilde{\mathbf{m}}$ are discarded until convergence is achieved, generally requiring no more than 10 iterations.

In order to make comparisons between each tested sample, we maintain the same relative weights in the inversion missfit function. The standard deviation σ_m from the *a priori* model m_{priori} is 0.53, which controls the degree of accuracy to which the measured data are fitted. The other free parameter in the inversion is the correlation distance between cells L_c which is set to 12.26 for all three tests. The wavefield diffusivity $\mathcal{D}$ in

eq. (2) is assumed to remain constant throughout each test, and is therefore estimated from a single trace selected at approximately 50 % of peak stress by the approach described in *Anugonda et al.* [2001]. This simplification is motivated by the observation of previous applications of CWD [*Zhang et al.*, 2018], that the inversion is relatively insensitive to changes in $\mathcal{D}$.

Additionally, each successive time-step in the inversion p is independent from one-another as the initial m_{priori} are set to zero. Therefore, any observed correlations between successive distributions of σ_{T_ρ} are derived from the input data $\mathbf{K}_p^m$. A total of four, non-overlapping 40 µs correlation windows beginning at 50 µs up to 210 µs within the coda are applied. The value of 50 µs is selected as this point corresponds to the onset of mostly diffusive decay in energy. The width of each correlation window must be significantly larger than the dominant period T_0 of the wavefield, while the number of windows must be balanced against computational cost.

The core volume is discretised into a tetrahedral mesh of 3.2 mm characteristic length [*Geuzaine and Remacle*, 2017], resulting in ~15 000 cells, thereby keeping the computational time low. The model parameters $\tilde{\mathbf{m}}$ resulting from each inversion time-step p are mapped onto the tetrahedral mesh, providing an indication of the spatio-temporal changes in the density of scattering cross-section σ_{T_ρ} with respect to the reference data cube D_{ref}. The reference point is selected towards the beginning of axial stress loading, once confining pressure has been applied, thereby ensuring each ultrasonic transducer is sufficiently coupled to the lateral surface of the WM sample (see fig. 1). Furthermore, in all cases a comparison is made between the $\tilde{\mathbf{m}}$ distribution resulting from: (i) a fixed reference comparison (i.e. consecutive correlations between D_{p_i} and D_{ref}); and (ii) the $\tilde{\mathbf{m}}$ distribution resulting from a rolling reference comparison, (i.e. consecutive correlations between D_{p_i} and D_{p_i-N} which lags behind p_i by N surveys). Where large changes in $\mathbf{K}_n^m$ are identified early on during a given deformation experiment, a second D_{ref} is defined in order to avoid large decorrelation and therefore a reduction in sensitivity to subsequent changes [*Zotz-Wilson et al.*, 2019].

3 Results

The analysis of the mudstone samples will be presented from highest to lowest water saturation, i.e., 70%, 58% and 28%. For each sample, the distribution of σ_{T_ρ} throughout

deformation is compared to the post-failure fracture network as imaged by post-mortem X-ray CT scanning. In order to quantitatively compare the three-dimensional inversion results with the evolution of stress during axial loading, 4 mm spheres are placed within the centre of regions of high σ_{T_ρ}; and the average value of all intersected tetrahedra is calculated for each survey/time step throughout the experiment. This allows direct quantitive comparison of the three-dimensional distribution of σ_{T_ρ} with the changes in differential stress.

In all cases, rolling reference monitoring is performed to ensure the rate-of-change in σ_{T_ρ} correlates with the fixed reference results, thereby avoiding a spurious correlation after sudden large or prolonged changes in the medium [*Zotz-Wilson et al.*, 2019]. For the samples of lower initial water saturation (58 % and 28 %), two fixed reference points before and after large changes in σ_{T_ρ} are defined. For the 70 % S_w sample, in which only a single large shear fracture formed (fig. 2.b), only a single reference point is necessary. For each deformation experiment we report the evolution of differential stress with time, including the 3 days of consolidation under isotropic stress preceding the axial loading stage.

Depending on the experiment, active source surveys were conducted every 2.3 min or 5 min. No acoustic emissions were detected during the (1.8 min or 4.5 min) period of passive monitoring between each consecutive active survey. Therefore, for the applied strain rate of $1 \times 10^{-7}\,\mathrm{s}^{-1}$, and saturation levels, the Whitby Mudstone is considered to produce no AE of sufficient magnitude to be detected.

3.0.1 Sample with 70 % initial water saturation

For the 70 % sample shown in fig. 2.a, an initial increase in σ_{T_ρ} occurs at the base of the main shear fracture (point A in fig. 2.b), which was identified from the post-mortem X-ray CT images. The changes in σ_{T_ρ} in region A relative to the fixed reference show an initial increase at 13.8 MPa or 36 % of the peak stress, see fig. 2.a. This initial increase peaks at 90 h, for a differential stress of ~20 MPa, before reducing again and reaching a local minimum of ~26 MPa at 98 h. This is immediately followed by a second sharp increase, around the onset of non-linear deformation. A third smaller rise occurs at ~106 h, followed by a smaller reduction up until ~113 h. A final slight increase in σ_{T_ρ} leading up to peak stress at 37.8 MPa occurs, followed by a slight drop coinciding with the point of

failure. This is followed by ~20 h of slip along the newly formed shear feature(s), during which σ_{T_ρ} shows a gradual increase, plateauing out towards the end of the experiment.

The rolling-reference dashed curve in region A (fig. 2.a) provides an indication of the rate-of-change in σ_{T_ρ} between surveys performed 4.22 h apart. This curve shows its largest value at 89 h followed by peaks of reducing magnitude coinciding with the increase noted in the fixed-reference results at 102 h and 108 h. This provides confidence in the fixed-reference distribution of σ_{T_ρ}. At the peak stress, a final larger increase in the rolling reference σ_{T_ρ} curve occurs.

The six snapshots taken at the plain disks • shown in fig. 2.a, display the σ_{T_ρ} distribution for both x-z slices (fig. 3), and slices parallel to the A-B fracture plane (fig. 4). For a movie of these figures covering the entire experiment see S3. The differences between the first two time-steps ($\bullet_1 - \bullet_2$) in both figures show a localised increase in σ_{T_ρ} towards the base of the post-deformation main shear fracture (A), with some distribution along the fracture plane (A-B). As stress increases, the point of largest σ_{T_ρ} moves further downward along the fracture plane, with the fracture tip also showing a region of increased σ_{T_ρ}, slightly skewed to the right side of the fracture plane, see point B in fig. 4. Further, there is a reduction in the distribution around point B and an increase in the extent at the fracture base (point A) before ($\bullet_4 - \bullet_5$) and after ($\bullet_5 - \bullet_6$) failure. The x-z slices (fig. 3) also capture the downward movement and increase in σ_{T_ρ} toward the base of the main fracture.

3.0.2 Sample with 58 % initial water saturation

The 58 % sample shows two post-deformation shear fractures. The main fracture extends from the lower right (A) of the x-z slice, up until ~58 mm on the left (B) as shown in fig. 5.b. The smaller fracture extends from the approximate centre of the x-z slice (C), up until ~35 mm (D). The CWD inversion results indicate an initial increase in σ_{T_ρ} coinciding with the upper end of the minor fracture (region D), peaking at ~100 h, see fig. 5.a. The distribution of this initial increase is captured at the ▲ snapshots, shown in fig. 6, or as a movie in S4. Between $\blacktriangle_1 - \blacktriangle_3$ upward drift in the location of maximum σ_{T_ρ} occurs, followed by an increase in both magnitude and spatial distribution from $\blacktriangle_4$-$\blacktriangle_5$. The final snapshot ($\blacktriangle_6$) shows the subsequent reduction in magnitude and spatial distribution. Just prior to the peak σ_{T_ρ} noted at 98 h along the minor fracture (region D curve in fig. 5.a),

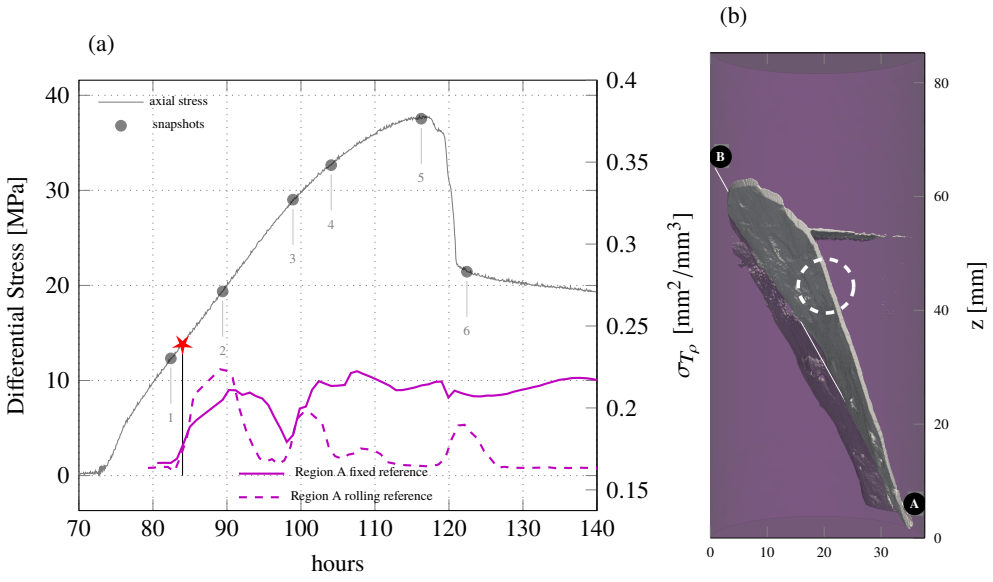

Figure 2. (a) Monitoring of the 70% S_w sample, showing the development in terms of scattering cross-section σ_{T_ρ} (reference at 80 h and the rate-of-change of σ_{T_ρ} (rolling reference lag of 4.22 h) for a 4 mm sampling sphere located at the base of the main shear fracture. The annotated ★ indicates the identified point at which σ_{T_ρ} first localises, while • indicate the snapshots displayed in figs. 3 and 4. (b) X-Ray post-deformation single shear fracture, with a horizontal pre-deformation dehydration fracture plane at ~55 mm. The dashed region was obscured during X-Ray tomography by a transducer and therefore represents an interpretation. See S2 for an isometric view rotation of the fracture network.

an increase occurs at both the base (region A curve) and tip (region B curve) of the major fracture. The six ■ snapshots shown in fig. 7 indicate a progressive increase in σ_{T_ρ} towards the major fracture tip (B), continuing all the way to peak stress at 51.3 MPa. The x-z sliced distribution reflecting the • snapshots generated from a reference at 90 h (fig. 8) show a process by which the region of largest σ_{T_ρ} alternates between regions corresponding to the post-deformation minor (D) and major fracture (A) ($\bullet_1$-$\bullet_4$), and then focuses at the main fracture just prior ($\bullet_5$) to, and after ($\bullet_6$) the point of dynamic failure. See S5 for a movie of both the x-z and major fracture slice.

3.0.3 Sample with 28 % initial water saturation

The 28 % sample post-deformation fracture network consists of one large shear fracture, traversing from the lower left to upper right of the x-z slice (A-B in fig. 9.b), with

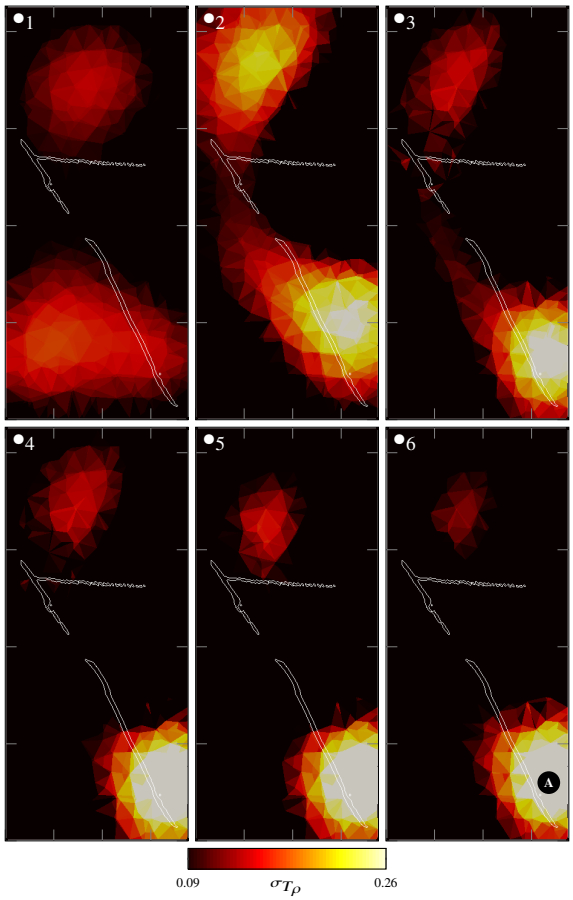

Figure 3. The 70% S_w sample sliced along the x-z plane for time steps $\bullet_1$ to $\bullet_6$ as indicated by the • symbols in fig. 2.a. Point A indicates the position of the 4 mm sampling sphere at $\bullet_6$. The distribution of σ_{T_ρ} initially localises at $\bullet_2$ and then drifts downward, displaying increased focus in region A, prior to ($\bullet_5$), and after ($\bullet_6$), failure. See S3 for a movie of this figure.

preexisting genetic dehydration fracture planes at the bottom (E) and two at the top (F) of the core. Around the base of the large fracture (A), several smaller fractures coalesce into a single fracture (C-D in fig. 9.b). Careful inspection of the post deformation X-Ray scans indicates several smaller fractures, most of which are on one side of the main shear fracture, though there also exists a smaller fracture which originates from two conical low density heterogeneities (E) at the base of the core. Furthermore, the dashed region in fig. 9.b from the base of the core up until the lower dehydration fracture at E, was damaged during testing and subsequently this region fell off when the core was extracted from the pressure vessel. For the first ~10 min of experimentation the applied strain rate is $1 \times 10^{-6}\,\mathrm{s}^{-1}$ up until 7 MPa of axial stress, after which it is reduced to $1 \times 10^{-7}\,\mathrm{s}^{-1}$ for

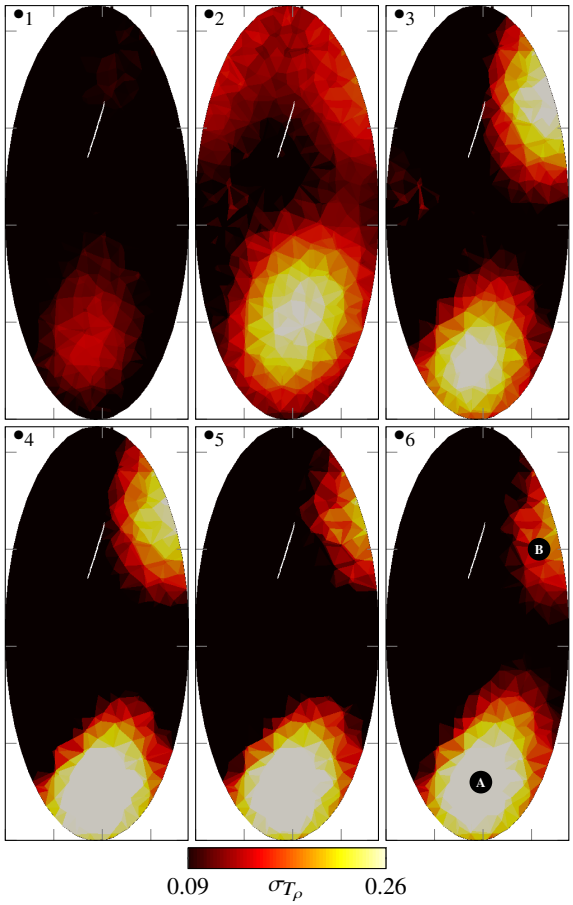

295 **Figure 4.** The 70% S_w sliced parallel to the fracture plane A-B, for time steps $\bullet_1$ to $\bullet_6$ as indicated by the
296 • symbols in fig. 2.a. Point A indicates the position of the 4 mm sampling sphere at t_6, while point B shows
297 the position of the maximum σ_{T_ρ} around the fracture tip. The distribution of σ_{T_ρ} initially localises at $\bullet_2$ and
298 then drifts downward, displaying increased focus in region A, prior to ($\bullet_5$), and after ($\bullet_6$), failure. See S3 for a
299 movie of this figure.

363 the remainder of the test. During this period of increased strain rate, in the centre region
364 of the minor fracture (C-D) an increase in σ_{T_ρ} occurs, the spatial distribution of which
365 is captured by the ■ snapshots indicated in fig. 9 and displayed in fig. 10. For a movie
366 of both figures see S6. While the first two time-steps $\blacksquare_1$ - $\blacksquare_2$ show almost the same dis-
367 tribution, the third $\blacksquare_3$ indicates an increase in magnitude and upward movement. This
368 is then followed ($\blacksquare_4$ - $\blacksquare_6$) by an increase in spatial distribution and magnitude of σ_{T_ρ}.
369 Shortly afterwards a subsequent reduction in σ_{T_ρ} occurs. In order to improve sensitivity to
370 subsequent changes, a reference point is defined at 105 h. The results from this redefined
371 reference show an increase in σ_{T_ρ} within a region coinciding with the two low density

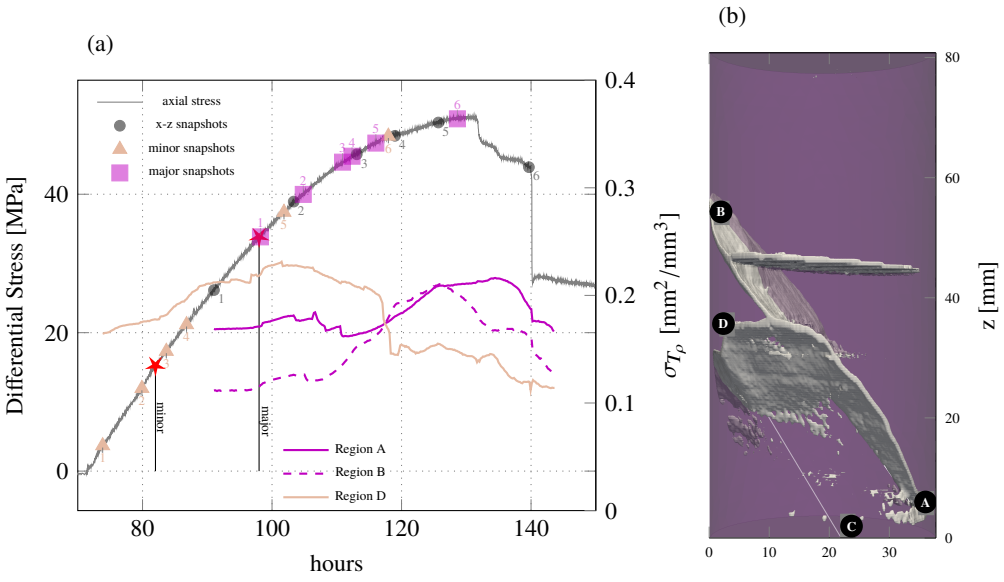

Figure 5. (a) Monitoring of the 58% S_w sample, showing the development in terms of scattering cross-section σ_{T_ρ} for three 4 mm spheres located within the minor and main shear fractures. The annotated ★ indicates the identified point at which σ_{T_ρ} first localises, while •, ▲, and ■ indicate the snapshots displayed in figs. 6 to 8. (b) X-Ray post-deformation major (A-B) and minor (C-D) shear fractures, with a preexisting dehydration fracture plane at ~45 mm. See S2 for an isometric view rotation of the fracture network.

heterogeneities (E), and in a region around the upper dehydration fractures (F). See the • snapshots indicated in fig. 9 and displayed in fig. 11. For a movie of both figures see S7. This centre of maximum σ_{T_ρ} around E moves downward as it increases ($\bullet_1$ - $\bullet_3$), up until 130 h, at which point a gradual reduction begins. During $\bullet_1$ - $\bullet_3$ we also note a region of increasing σ_{T_ρ} around the upper dehydration fracture F. After peak stress is reached at ~167 h a rapid redistribution of σ_{T_ρ} over the main fracture plane occurs (Region A curve in fig. 9.a), which increases post failure, between $\bullet_5$ and $\bullet_6$. This re-activation of the region surrounding the main fracture plane is spatially captured by the □ snapshots shown in fig. 12 and movie in S7, which shows minimal increase between $\square_1$ and $\square_2$ prior to peak stress, followed by increased distribution $\square_3 - \square_6$ after failure.

3.0.4 Comparative analysis

For each of the samples of varying initial S_w, an initial increase in σ_{T_ρ} is determined, based on the criterion of an increase in both its rate-of-change and spatial focus.

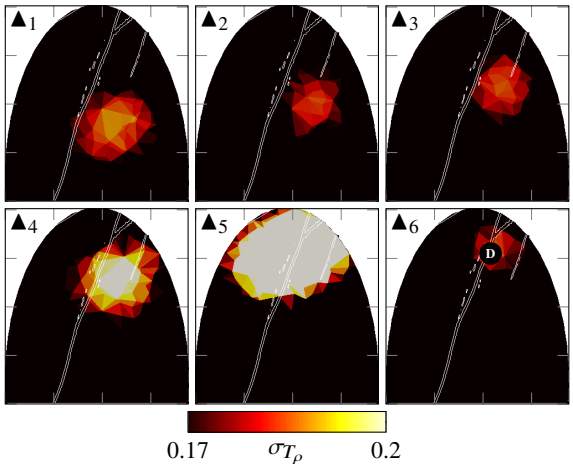

Figure 6. The 58% S_w sample sliced along the minor fracture plane C-D, for time steps ▲$_1$ to ▲$_6$ as indicated by the ▲ symbols in fig. 5.a. Point D indicates the position of the 4 mm sampling sphere at t_6. The focal point of the distribution of σ_{T_ρ} moves upwards between ▲$_1$ and ▲$_3$ and then increases in magnitude and spatial extent between ▲$_4$ and ▲$_5$. Subsequent reduction in the magnitude of σ_{T_ρ} occurs towards ▲$_6$. See S4 for a movie of this figure.

This point is marked in figures figs. 2, 5 and 9 by a ★. For both the 70 and 58 % S_w samples an increase in localised σ_{T_ρ} is found at ~14 MPa, while for the 28 % S_w this occurs at 6.5 MPa, see fig. 13. Additionally, we identify a negative correlation between S_w and the peak differential stress achieved during each test [*Douma et al.*, 2019].

The relationship between the differential stress normalised by each sample peak stress with volumetric strain is shown in fig. 14. All core samples show an initially positive compactive response though become dilative prior to failure. Here both the 70 % and 58 % S_w samples show the identified initial focus in σ_{T_ρ} (★) to occurs within the compactive region, prior to the onset of dilatancy.

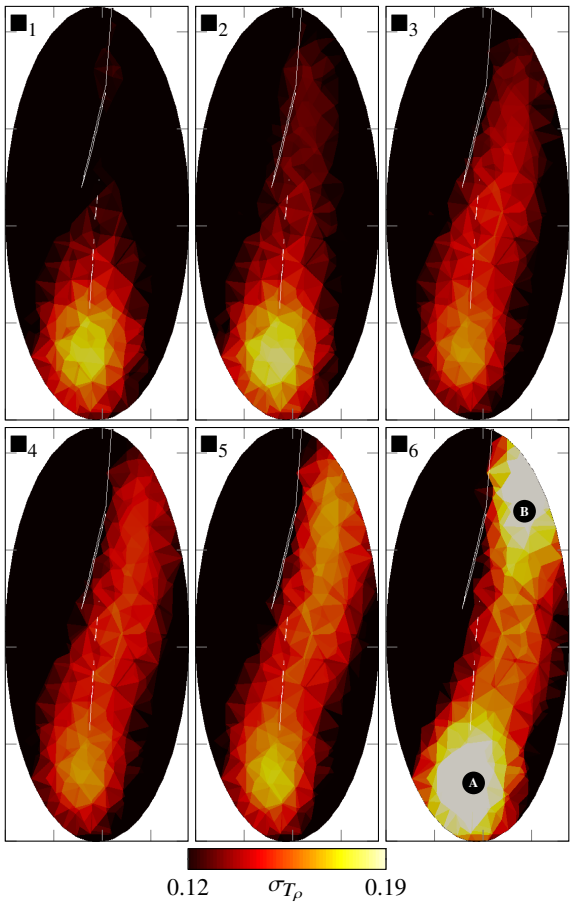

Figure 7. The 58% S_w sample sliced along the fracture plane A-B, for time steps ■$_1$ to ■$_6$ as indicated by the ■ symbols in fig. 5.a. Points A and B indicate the position of the 4 mm sampling sphere at t_6. The distribution of σ_{T_ρ} increases from point A towards point B between ▲$_1$ and ▲$_6$. A notable increase in its magnitude at both A and B occurs at ▲$_6$. See S4 for a movie of this figure.

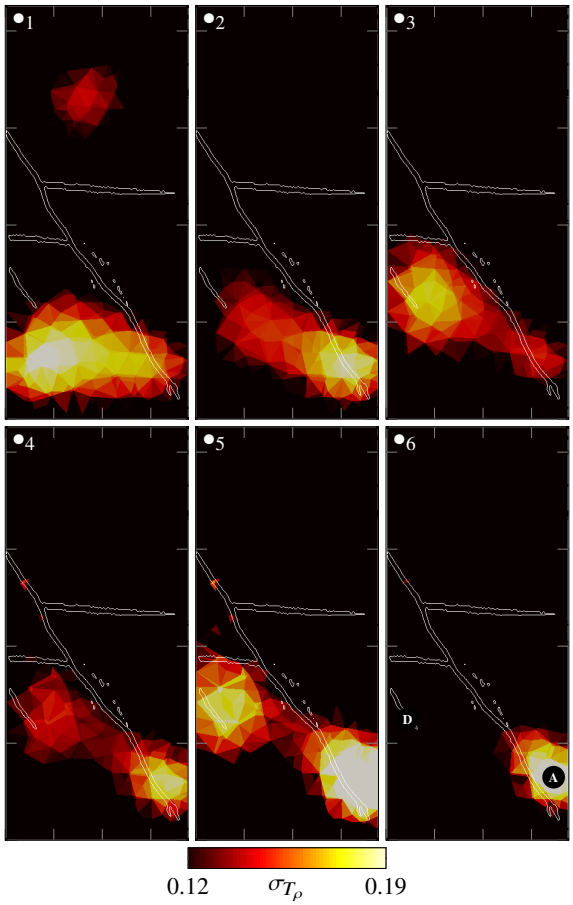

Figure 8. The 58% S_w sample sliced along the x-z plane for time steps $\bullet_1$ to $\bullet_6$ as indicated by the • symbols in fig. 5.a, and a reference at 90 h. Points A and D indicate the position of the 4 mm sampling spheres at t_6. The distribution of σ_{T_ρ} alternates between region D and A twice ($\bullet_1$ to $\bullet_4$). At $\bullet_5$ prior to failure, region A shows greater σ_{T_ρ} than region D. After failure at $\bullet_6$ only region A displays a focused region of σ_{T_ρ}. See S4 for a movie of this figure.

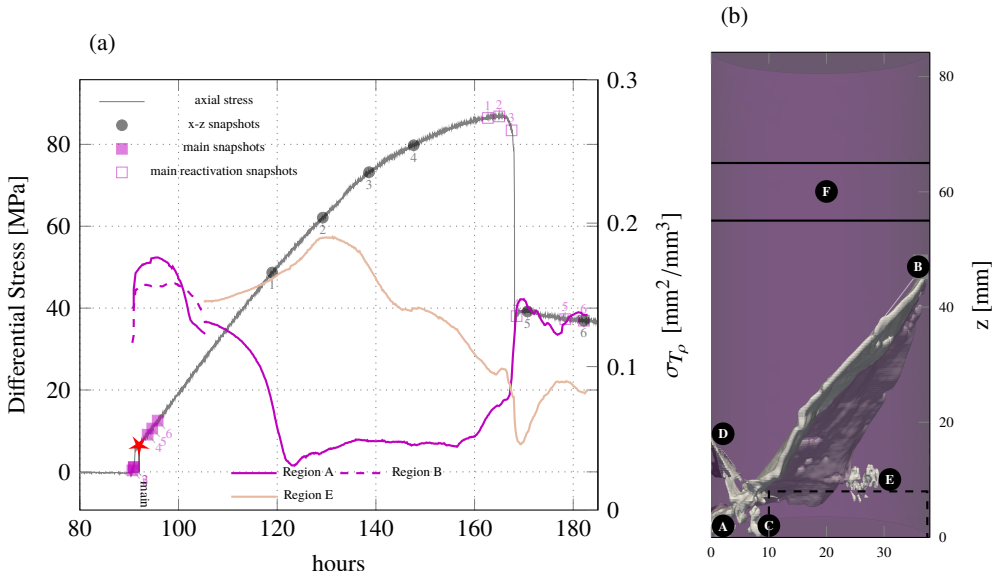

Figure 9. (a) Monitoring of the 28% S_w sample, showing the development of σ_{T_ρ} at the base and tip of the main fracture, and in a region surrounding the high-density impurities. Note the dashed, Region B curve is only shown for the fixed-reference distribution at the beginning of the stress increase. The annotated ★ indicates the identified point at which σ_{T_ρ} first localises, while •, ■, and □ indicate the snapshots displayed in figs. 10 to 12. (b) X-Ray post-deformation major (A-B) and minor (C-D) shear fractures, with preexisting dehydration fracture planes above and below F, and below E. Two low-density impurities present in the sample are indicated at point E. The dashed regions below E was damaged during testing, and therefore was not present during X-Ray tomography. See S2 for an isometric view rotation of the fracture network.

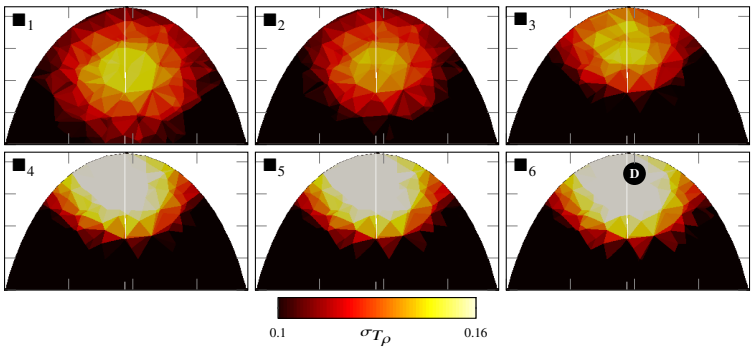

Figure 10. The 28% S_w sample sliced along the minor fracture plane C-D, for time steps ■$_1$ to ■$_6$ as indicated by the ■ symbols in fig. 9.Point D indicates the position of the 4 mm sampling sphere at t_6. The focal point of the distribution of σ_{T_ρ} moves upward between ■$_1$ and ■$_3$, and then increases in magnitude between ■$_4$ and ■$_6$. See S6 for a movie of this figure.

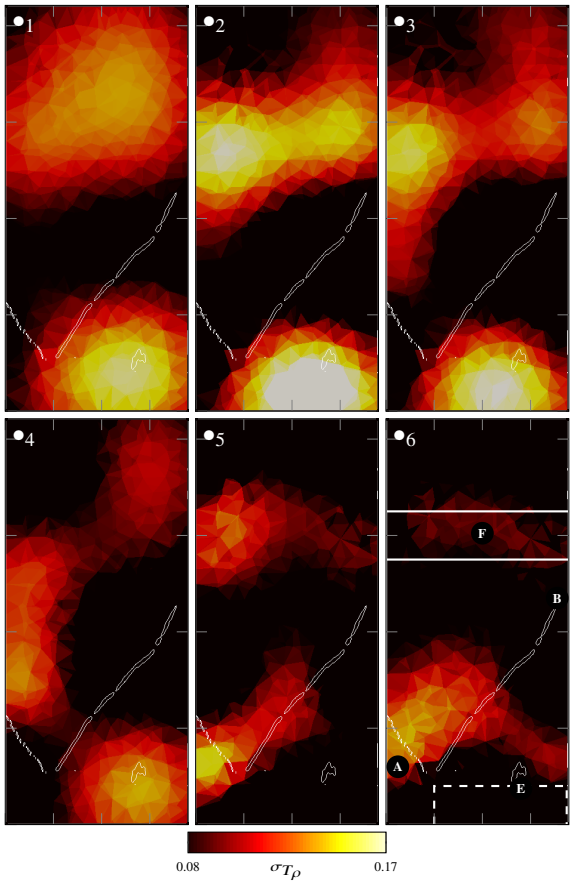

Figure 11. The 28% S_w sample sliced along the x-z plane for time steps $\bullet_1$ to $\bullet_6$ as indicated by the $\bullet$ symbols in fig. 9. Points A and E indicate the position of the 4 mm sampling spheres at t_6. Point F indicates the dehydration planes; point E the low density inhomogeneities; and B the main fracture tip. Between $\bullet_1$ and $\bullet_3$ the σ_{T_ρ} distribution increases in magnitude and focus around regions E and F. At $\bullet_4$ a reduction in both regions magnitude and distribution occurs. The post failure snapshots ($\bullet_5$ to $\bullet_6$) show distribution from region A towards region B and within region F. See S7 for a movie of this figure.

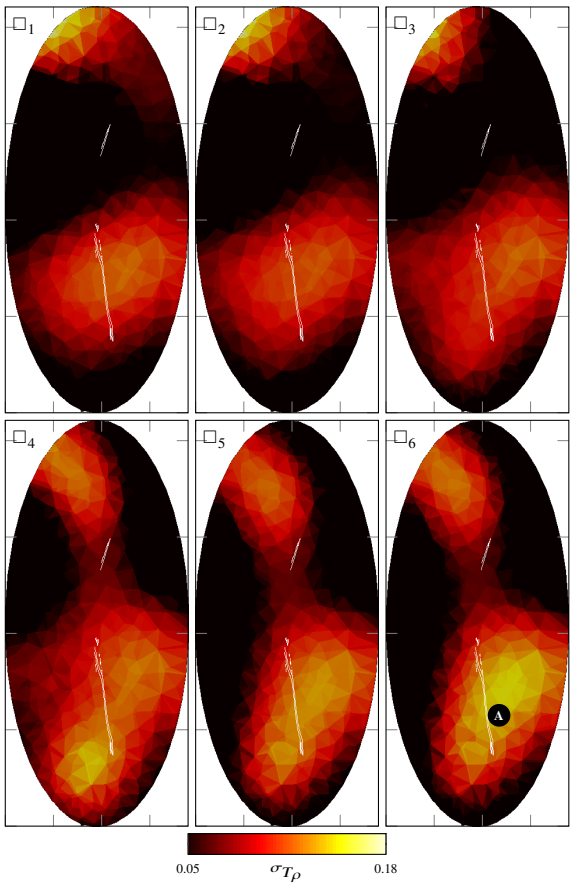

Figure 12. The 28% S_w sample sliced along the main fracture plane A-B, for time steps $\square_1$ to $\square_6$ as indicated by the □ symbols in fig. 9. Point A indicates the position of the 4 mm sampling sphere at t_6. Between $\square_1$ and $\square_3$ there is a slight increase in the σ_{T_ρ} distribution in region A, while between $\square_3$ and $\square_4$ a rapid increase occurs cross the plain A-B. From $\square_4$ and $\square_6$ the magnitude σ_{T_ρ} increases in region A. See S7 for a movie of this figure.

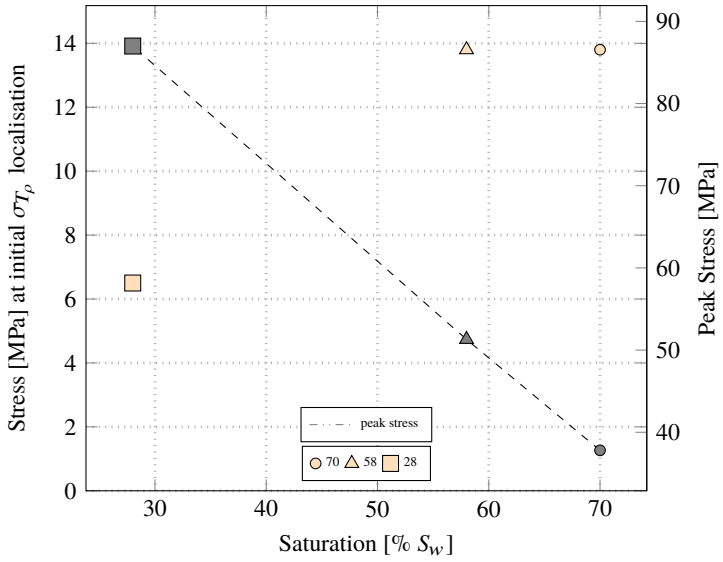

412 **Figure 13.** Comparison between the interpreted onset of localised inelastic strain on the left axis, and
413 differential peak stress on the right axis, vs initial water saturation of each core sample.

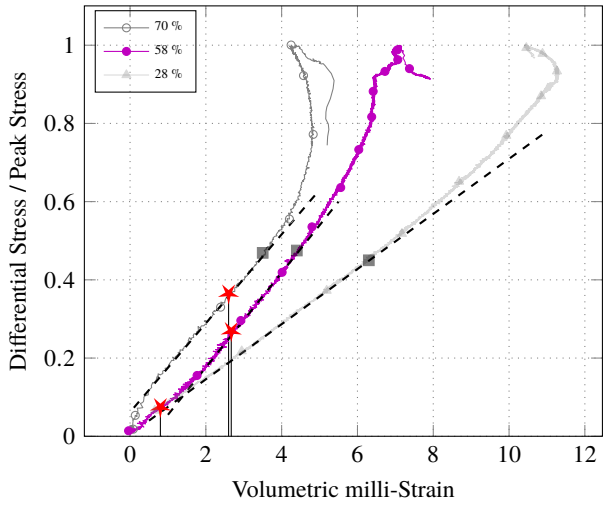

414 **Figure 14.** The differential stress, normalised by each samples peak stress, is compared with the volumetric
415 milli-strain. The point of identified initial localisation in σ_{T_ρ} is indicated by ★, which for the 70 % and 58
416 % samples occurs within a region of approximately linear change, prior to the onset of dilatancy which is
417 identified by the ■ symbols.

4 Discussion

4.1 The development of the fracture network as interpreted from the distribution of scattering cross-section

The application of CWD inversion in monitoring the triaxial deformation of three mudstones of varying initial water saturation, indicates progressive and repeated re-distribution of inelastic strain within the rock following strain localisation events. Here we define microscopic inelastic strain as associated with closure, opening or shearing along microscopic fractures, while macroscopic inelastic strain refers to the coalescence of microscopic cracks into a large shear fracture. A region of increased σ_{T_ρ} indicates initial localised microscopic inelastic strain and eventually the formation of macroscopic fractures. An increase in spatial distribution indicates the growth of a cracked region, while the increase in magnitude of σ_{T_ρ} indicates either an increase in the crack density and/or an increase in the impedance contrast between the cracks and the rock matrix, which can be interpreted as a change in the aperture of the cracks/fractures.

For the most saturated sample, there are three stages of increase, followed by a decrease in σ_{T_ρ} at the base of the main shear fracture (point A in fig. 2.b). This suggests initial localised strain occurs, which is subsequently closed as the stress is reduced and redistributed throughout the rest of the sample. The reactivation of the same region and the increase in both the distribution (spatial extent) and magnitude of σ_{T_ρ} suggests an increase occurs in the width, and aperture of the fracture, respectively. This is evident when viewing the slice along the fracture plane (fig. 4 or the S.3 movie), where only after reactivation at 98 h ($\bullet_3$) does the spatial distribution of σ_{T_ρ} notably increase at both the base (A) and tip (B) of the fracture. This coincides with the onset of non-linear inelastic deformation or the yield point of the sample. The subsequent reduction in σ_{T_ρ} distribution at the tip (B) and increase at the base (A) before ($\bullet_4 - \bullet_5$), and after ($\bullet_5 - \bullet_6$) failure, indicates that the fracture plane grows laterally at the base while the tip closes up. Further, the observed reduction in the maximum rate-of-change in σ_{T_ρ} over the first three activations at the fracture base (dashed curve in fig. 2.a) suggests a linear reduction in the rate at which the micro/macroscopic fractures open.

The distribution of σ_{T_ρ} during the 58 % S_w test also displays a process of continuous re-distribution of stress, though in this case between a region corresponding to the minor (C-D) and major (A-B) fractures in fig. 5.b. Initially, in a region surrounding the

minor fracture (C-D) at ~82 h, we interpret the formation of microscopic inelastic strain. Growth occurs in both magnitude and distribution at ~89 h (see ▲$_4$ in fig. 6 or S.4 movie), indicating larger scale coalescence occurs at this point. At 98 h, the main fracture appears to initiate, from the base (A) which again corresponds to the classically determined yield point of the sample. With continued deformation the σ_{T_ρ} distribution moves towards the tip (B), and eventually fails the sample. Throughout the test we identify approximately four stages of redistribution in σ_{T_ρ} (see •$_1$ − •$_4$ in fig. 8 or S.5 movie) between the minor and major fracture. This is interpreted as several stages of opening and closure of initially microscopic and eventually macroscopic fractures, as stress redistribution occurs.

The sample with the lowest initial water content (28 %S$_w$) with its major (A-B in fig. 9.b), and minor (C-D) fractures, show a similar process of re-distribution of σ_{T_ρ}. However, a notable difference with this sample is the presence of the two low density, approximately conical heterogeneities (region E in fig. 9.b) at the lower end of the core. These are interpreted as the void left by the exoskeleton of gastropods such as the Neptunea contraria [*Linnaeus*, 1771]. The distribution of σ_{T_ρ} supports an interpretation where initially the minor fracture (C-D) experiences localised strain at the base of the core, during the initial region of increased strain-rate, see snapshots ■ in (fig. 10) or S6 movie. This is followed by gradual prolonged fracturing of a large region surrounding the low density impurities, see •$_1$ − •$_4$ in fig. 11 or the S.7 movie. Subsequently the major shear fracture (A-B) develops (□$_4$ − □$_6$ in fig. 12 and •$_5$ − •$_6$ in fig. 11 or the S.7 movie) close to the peak stress, and the failure of the sample. This interpretation is supported by the fact that the region surrounding the interpreted marine exoskeletons (E) was fractured to the point that it fell off the end of the sample once removed from the pressure vessel. Additionally, the concentration in σ_{T_ρ} between the two preexisting dehydration fractures (F), particularly between •$_2$ − •$_3$ in fig. 11, indicates that either a change in compliance occurs over these interfaces, or microscopic changes occur within the region between them (a layer of different mineralogy or microstructure).

In summary, for all tested samples the identified localisation in σ_{T_ρ} was found early on during deformation, between 7 % and 36 % of the peak differential stress and prior the onset of dilatancy (see fig. 14). We therefore interpret this initial localisation in σ_{T_ρ}, not as the formation of macroscopic coalesced shear fractures but primarily driven by distributed intergranular opening, closure, and shearing at the microscopic scale. A similar conclusion was reached in a recent study by *McBeck et al.* [2018] on the Green River

shale, during which core samples were time-lapse imaged by X-Ray microtomography while under confining pressure. The identification of localised strain regions became apparent at 35 % of the peak differential stress, preceding macroscopic shear failure. This value is consistent with the upper limit of the range reported here. The interpretation of microscopic fracture formation within the inelastic region (before dilatancy) for WM samples is supported by *Douma et al.* [2019], where non-elastic wave-speed changes were observed, conducive with microfracturing. Further, *McBeck et al.* [2018] demonstrate that microscopic opening, closure, and shearing work together to eventually produce macroscopic shear failure. Their observations support our interpretation of a complex timeline of locally increasing (opening or shearing) and decreasing (closure of micro/macroscopic fracturing) σ_{T_ρ} up until failure.

It is also interesting to note that the observed initial distribution of σ_{T_ρ} in the x-z snapshots shows similar contours to the expected maximum regions of elastic stress distribution for a cylindrical core (2:1 length to diameter ratio) as described by *Paterson and Wong* [2005]. While this is most evident at the beginning of the S3 and S6 movies, it is also shown by the $\bullet_1$ snapshot in fig. 3.

4.2 The impact of water saturation

The Whitby Mudstone plugs display an increase in strength and a reduction in plasticity with a reduction in water saturation [*Douma et al.*, 2019] . The primary mechanism driving these changes is expected to be an increase in the capillary suction within the pore space of the mudstone [*Fjar et al.*, 2008; *Ramos da Silva et al.*, 2008; *Ferrari et al.*, 2014]. As the pore-fluid evaporates from the mudstone, a reduction in the pore-pressure occurs, leading to a tensile stress or negative pressure, and finally a change in compliance (or stiffness) between individual grains [*Onaisi et al.*, 1994; *Forsans and Schmitt*, 1994; *Ewy*, 2014]. This ultimately leads to an increase in the strength and a reduction in the plasticity of the material. Our experimental results corroborate this relationship which has been recently confirmed for the Whitby Mudstone [*Douma et al.*, 2019] as well as other mudstones [*Vales et al.*, 2004; *Ramos da Silva et al.*, 2008; *Ghorbani et al.*, 2009]. The failure of the partially-saturated Whitby Mudstone occurs in the brittle domain, where shear failure of the result in the formation of dilative fracture planes [*Douma et al.*, 2019]. Furthermore, the comparison between the identified onset of inelastic strain (microscopic damage), and initial water saturation suggests a non-linear relationship, see fig. 13. However,

this may be also due to the added inhomogeneity of the low S_w sample (the low density heterogeneity), or the higher initial strain-rate, and therefore more measurement points are required to statistically validate this argument.

As no AE were detected during passive monitoring of the samples, this suggests that the brittle failure necessary to generate AE is insufficient [*Main*, 1990] to overcome the environmental noise.

4.3 CWD: An effective real-time fracture monitoring tool

This study on samples from the WMF indicates that CWD inversion has the potential to image the initiation, propagation and branching of fractures or other heterogeneities, tested under realistic subsurface conditions (stress, pressure, temperature). While there are several other techniques which provide spatio-temporal information on inelastic strain at in-situ conditions, they often require substantial investment in equipment and post-processing, or are inherently less sensitive to subtle localised microscopic changes.

Time-lapse synchrotron micro-tomography undoubtedly provides the highest spatial resolution, as it is able to resolve the detailed structure of macroscopic fractures [*Renard et al.*, 2017, 2018], and microscopic strain localisation through digital volume correlations [*Kandula et al.*, 2018; *Mao et al.*, 2019; *Mao and Chiang*, 2016; *McBeck et al.*, 2018]. The main limitation of this method is that it requires access to an X-ray beam in a synchrotron of sufficient energy to image a sample housed within a bespoke pressure vessel. Further, the maximum sample size is strictly constrained by both the spatial and temporal resolution requirements.

Traditional acoustic imaging methods such as velocity tomography, while more affordable, and able to provide sufficient spatiotemporal resolution to resolve the region around macroscopic fractures [*Jansen et al.*, 1993; *Brantut*, 2018; *Aben et al.*, 2019], have not shown sensitivity to microscopic inelastic strain localisation.

Passive AEs monitoring is a well established technique in experimental rock mechanics, and with a sufficiently accurate velocity model provides a spatio-temporal indication of the occurrence of brittle failure [*Lei et al.*, 2004; *Aben et al.*, 2019; *Brantut*, 2018; *Jansen et al.*, 1993; *Sarout et al.*, 2017]. However, as demonstrated by this study on the WMF, AEs monitoring relies on the existence of seismicity of sufficient magnitude and

frequency to be detected by the available sensor network. For clay- or calcite-rich rocks, where inelastic deformation can develop in a plastic, relatively silent fashion [*Peng and Yang*, 2018], AEs monitoring is a less suitable method to determine the onset of inelastic strain. Further, both active and passive monitoring methods require time consuming pre-processing steps, such as first arrival picking, and the construction of a velocity model, thereby limiting their utility in real-time monitoring.

In summary, CWD inversion monitoring requires little to no additional investment in equipment where acoustic monitoring is already available. Further, it is more sensitive to subtle changes in scattering or velocity than methods which rely on the coherent arrivals [*Zotz-Wilson et al.*, 2019], and once appropriate inversion parameters are determined for a particular lithology and receiver arrangement, quasi-real-time monitoring is feasible. While CWD inversion cannot provide the same spatial resolution as synchrotron micro-tomography, it appears to demonstrate similar sensitivity to the onset of microscopic inelastic strain. There also exist considerable opportunity to improve upon the application CWD within the laboratory setting. For example, the sensitivity kernels used in this study (eq. (2)) do not account for the core boundaries, any in-situ heterogeneities, or the anisotropic layered nature of the WMF. Several works have proposed to better account for the initial material state by first determining the sensitivity kernels by numerically modelling of the diffusive propagation of energy within [*Kanu and Snieder*, 2015; *Xue et al.*, 2019].

5 Conclusion

The CWD inversion monitoring of the Whitby Mudstone during triaxial compaction, indicates that the formation of inelastic strain localisation occurs at less than 36 % of peak stress. The AE monitoring suggest such inelastic localisations develop gradually not impulsively, from microscopic diffuse damage, up until the macroscopic shear failure, while the comparison of different S_w suggests a non-linear relationship with the onset of strain localisation. In general, the application of CWD inversion to what is ostensibly an aseismic mudstone, has enabled a qualitative discussion of the time and location at which initial microscopic inelastic strain (opening, closure, and shearing) develops. Furthermore, subsequent stages of reactivation and eventual macroscopic shear failure are discernible.

Acknowledgments

We would like to thank David Nguyen and Stephen Firns at CSIRO's Geomechanics and Geophysics Laboratory, for their assistance during the experimentation. The assistance provided by Joost Van Meel at TUDelft in post processing the CT-scans is also much appreciated. Further, the funding provided by the Dutch Upstream Gas top-sector initiative (project TKIG01020) and our industry partners Energie Beheer Nederland B.V., and Neptune Energy Netherlands B.V., Wintershall Noordzee B.V. is acknowledged. Furthermore, we would like to acknowledge the use of the open-source python module pyVista [*Sullivan and Kaszynski*, 2019], which is used to visualise all of the 3-D fracture networks, and CWD inversion results. The raw acoustic and mechanical data used in this study is available at *Zotz-Wilson et al.* [2019], under the name "Acoustic, mechanical, and microstructure data used in: Ultrasonic Imaging of the Onset and Growth of Fractures within Partially Saturated Whitby Mudstone using Coda-Wave Decorrelation Inversion".

References

Aben, F. M., N. Brantut, T. M. Mitchell, and E. C. David (2019), Rupture Energetics in Crustal Rock From Laboratory-Scale Seismic Tomography, *Geophys. Res. Lett.*, doi: 10.1029/2019GL083040.

Aikas, T., and R. Sundell (2014), ONKALO - From Concept to Reality, 1, pp. 1–9, WM2014 Conference, Phoenix,.

Anugonda, P., J. S. Wiehn, and J. A. Turner (2001), Diffusion of ultrasound in concrete, *Ultrasonics*, *39*(6), 429–435, doi:10.1016/S0041-624X(01)00077-4.

Aplin, A. C., and J. H. Macquaker (2011), Mudstone diversity: Origin and implications for source, seal, and reservoir properties in petroleum systems, *Am. Assoc. Pet. Geol. Bull.*, doi:10.1306/03281110162.

Armitage, P. J., R. H. Worden, D. R. Faulkner, A. R. Butcher, and A. A. Espie (2016), Permeability of the Mercia Mudstone: suitability as caprock to carbon capture and storage sites, *Geofluids*, *16*(1), 26–42, doi:10.1111/gfl.12134.

Ayalew, L., and H. Yamagishi (2005), The application of GIS-based logistic regression for landslide susceptibility mapping in the Kakuda-Yahiko Mountains, Central Japan, *Geomorphology*, *65*(1-2), 15–31, doi:10.1016/j.geomorph.2004.06.010.

Brantut, N. (2018), Time-resolved tomography using acoustic emissions in the laboratory, and application to sandstone compaction, *Geophys. J. Int.*, pp. 2177–2192, doi:

612 10.1093/gji/ggy068.

613 Brookins, D. G. (1976), Shale as a repository for radioactive waste: The evidence from
614 Oklo, *Environ. Geol.*, *1*(5), 255–259, doi:10.1007/BF02676715.

615 Busch, A., S. Alles, Y. Gensterblum, D. Prinz, D. Dewhurst, M. Raven, H. Stanjek, and
616 B. Krooss (2008), Carbon dioxide storage potential of shales, *Int. J. Greenh. Gas Con-*
617 *trol*, *2*(3), 297–308, doi:10.1016/j.ijggc.2008.03.003.

618 Douma, L. A. N. R., J. Dautriat, J. Sarout, D. N. Dewhurst, and A. Barnhoorn (2019),
619 Impact of water saturation on the elastic anisotropy of the Whitby Mudstone, United
620 Kingdom, *GEOPHYSICS*, pp. 1–82, doi:10.1190/geo2019-0004.1.

621 Ewy, R. T. (2014), Shale swelling/shrinkage and water content change due to im-
622 posed suction and due to direct brine contact, *Acta Geotech.*, *9*(5), 869–886, doi:
623 10.1007/s11440-013-0297-5.

624 Ferrari, A., V. Favero, P. Marschall, and L. Laloui (2014), Experimental analysis of
625 the water retention behaviour of shales, *Int. J. Rock Mech. Min. Sci.*, *72*, 61–70, doi:
626 10.1016/j.ijrmms.2014.08.011.

627 Fjar, E., R. Holt, A. M. Raaen, R. Risnes, and P. Horsrud (2008), *Petroleum related rock*
628 *mechanics*, 2nd ed., 251 – 287 pp., Elsevier Sience.

629 Forsans, T. M., and L. Schmitt (1994), Capillary forces: The neglected factor in shale in-
630 stability studies?, *Soc. Pet. Eng. - Rock Mech. Pet. Eng. 1994*, pp. 71–84.

631 Garrels, R. M., and F. T. Mackenzie (1969), Sedimentary Rock Types: Relative Propor-
632 tions as a Function of Geological Time, *Science (80-.).*, *163*(3867), 570–571, doi:
633 10.1126/science.163.3867.570.

634 Geuzaine, C., and J.-F. Remacle (2017), A three-dimensional finite element mesh genera-
635 tor with built-in pre- and post-processing facilities, *Int. J. Numer. Meth. Engng.*

636 Ghorbani, A., M. Zamora, and P. Cosenza (2009), Effects of desiccation on the elas-
637 tic wave velocities of clay-rocks, *Int. J. Rock Mech. Min. Sci.*, *46*(8), 1267–1272, doi:
638 10.1016/j.ijrmms.2009.01.009.

639 Grêt, A. (2005), Monitoring rapid temporal change in a volcano with coda wave interfer-
640 ometry, *Geophys. Res. Lett.*, *32*(6), L06,304, doi:10.1029/2004GL021143.

641 Grêt, A., R. Snieder, and J. Scales (2006), Time-lapse monitoring of rock proper-
642 ties with coda wave interferometry, *J. Geophys. Res. Solid Earth*, *111*(3), 1–11, doi:
643 10.1029/2004JB003354.

Heap, M. J., P. Baud, P. G. Meredith, A. F. Bell, and I. G. Main (2009), Time-dependent brittle creep in darley dale sandstone, *J. Geophys. Res. Solid Earth*, *114*(7), 1–22, doi: 10.1029/2008JB006212.

Houben, M., A. Barnhoorn, L. Wasch, J. Trabucho-Alexandre, C. Peach, and M. Drury (2016a), Microstructures of Early Jurassic (Toarcian) shales of Northern Europe, *Int. J. Coal Geol.*, *165*, 76–89, doi:10.1016/j.coal.2016.08.003.

Houben, M. E., A. Barnhoorn, J. Lie-A-Fat, T. Ravestein, C. J. Peach, and M. R. Drury (2016b), Microstructural characteristics of the Whitby Mudstone Formation (UK), *Mar. Pet. Geol.*, *70*, 185–200, doi:10.1016/j.marpetgeo.2015.11.011.

Izumi, K., M. Ogihara, and H. Kameyaf (1998), *Displacements of bridge foundations on sedimentary soft rock: A case study on small-strain stiffness*, pp. 233–246, doi: 10.1680/pdbog.26421.0016.

Jansen, D. P., S. R. Carlson, R. P. Young, and D. A. Hutchins (1993), Ultrasonic imaging and acoustic emission monitoring of thermally induced microcracks in Lac du Bonnet granite, *J. Geophys. Res.*, *98*(B12).

Jianghui, M., Z. Min, Z. Hongjing, L. Luofu, W. Zhiyong, Z. Jieli, and W. Ying (2012), Geochemical Evidence for Coal and Carbonaceous Mudstone as the Possible Major Oil Source Rock in the Jurassic Turpan Basin, Northwest China, *Acta Geol. Sin. - English Ed.*, *86*(5), 1171–1181, doi:10.1111/j.1755-6724.2012.00739.x.

Kandula, N., B. Cordonnier, D. K. Dysthe, J. R. Sanchez, X. Zheng, F. Renard, W. Zhu, M. Kobchenko, J. McBeck, P. Meakin, C. Noiriel, and F. Fusseis (2018), Dynamic In Situ Three-Dimensional Imaging and Digital Volume Correlation Analysis to Quantify Strain Localization and Fracture Coalescence in Sandstone, *Pure Appl. Geophys.*, *C*, doi: 10.1007/s00024-018-2003-x.

Kanu, C., and R. Snieder (2015), Numerical computation of the sensitivity kernel for monitoring weak changes with multiply scattered acoustic waves, *Geophys. J. Int.*, *203*(3), 1923–1936, doi:10.1093/gji/ggv391.

Laloui, L., S. Salager, and M. Rizzi (2013), Retention behaviour of natural clayey materials at different temperatures, *Acta Geotech.*, *8*(5), 537–546, doi:10.1007/s11440-013-0255-2.

Larose, E., and S. Hall (2009), Monitoring stress related velocity variation in concrete with a 2E10-5 relative resolution using diffuse ultrasound, *J. Acoust. Soc. Am.*, *125*(4), 1853–1856, doi:10.1121/1.3079771.

Larose, E., J. De Rosny, L. Margerin, D. Anache, P. Gouedard, M. Campillo, and B. Van Tiggelen (2006), Observation of multiple scattering of kHz vibrations in a concrete structure and application to monitoring weak changes, *Phys. Rev. E - Stat. Nonlinear, Soft Matter Phys.*, doi:10.1103/PhysRevE.73.016609.

Larose, E., T. Planès, V. Rossetto, and L. Margerin (2010), Locating a small change in a multiple scattering environment, *Appl. Phys. Lett.*, *96*(20), doi:10.1063/1.3431269.

Larose, E., A. Obermann, A. Digulescu, T. Planès, J.-F. Chaix, F. Mazerolle, and G. Moreau (2015), Locating and characterizing a crack in concrete with diffuse ultrasound: A four-point bending test, *J. Acoust. Soc. Am.*, *138*(1), 232–241, doi:10.1121/1.4922330.

Lei, X., K. Masuda, O. Nishizawa, L. Jouniaux, L. Liu, W. Ma, T. Satoh, and K. Kusunose (2004), Detailed analysis of acoustic emission activity during catastrophic fracture of faults in rock, *J. Struct. Geol.*, *26*(2), 247–258, doi:10.1016/S0191-8141(03)00095-6.

Linnaeus, C. (1771), Mantissa Plantarum, *Mantissa Plant.*

Lockner, D. (1993), The role of acoustic emission in the study of rock fracture, *Int. J. Rock Mech. Min. Sci. Geomech. Abstr.*, *30*(7), 883–899, doi:10.1016/0148-9062(93)90041-B.

Main, I. G. (1990), Quasi-static modelling of stress histories during the earthquake cycle: precursory seismic and aseismic stress release, *Geophys. J. Int.*, *102*(1), 195–203, doi:10.1111/j.1365-246X.1990.tb00541.x.

Mao, L., and F.-p. Chiang (2016), 3D strain mapping in rocks using digital volumetric speckle photography technique, *Acta Mech.*, *227*(11), 3069–3085, doi:10.1007/s00707-015-1531-z.

Mao, L., H. Liu, Y. Zhu, Z. Zhu, R. Guo, and F.-p. Chiang (2019), 3D Strain Mapping of Opaque Materials Using an Improved Digital Volumetric Speckle Photography Technique with X-Ray Microtomography, *Appl. Sci.*, *9*(7), 1418, doi:10.3390/app9071418.

McBeck, J., M. Kobchenko, S. A. Hall, E. Tudisco, B. Cordonnier, P. Meakin, and F. Renard (2018), Investigating the Onset of Strain Localization Within Anisotropic Shale Using Digital Volume Correlation of Time-Resolved X-Ray Microtomography Images, *J. Geophys. Res. Solid Earth*, *123*(9), 7509–7528, doi:10.1029/2018JB015676.

Obermann, A., T. Planès, E. Larose, and M. Campillo (2013), Imaging preeruptive and coeruptive structural and mechanical changes of a volcano with ambient seismic noise,

J. Geophys. Res. Solid Earth, *118*(12), 6285–6294, doi:10.1002/2013JB010399.

Obermann, A., B. Froment, M. Campillo, E. Larose, T. Planès, B. Valette, J. H. Chen, and Q. Y. Liu (2014), Seismic noise correlations to image structural and mechanical changes associated with the Mw 7 . 9 2008 Wenchuan earthquake, *J. Geophys. Res. Solid Earth*, *119*(4), 3155–3168, doi:10.1002/2013JB010932.Received.

Obermann, A., T. Planès, E. Larose, and M. Campillo (2019), 4-D Imaging of Subsurface Changes with Coda Waves: Numerical Studies of 3-D Combined Sensitivity Kernels and Applications to the M_{w} 7.9, 2008 Wenchuan Earthquake, *Pure Appl. Geophys.*, *176*(3), 1243–1254, doi:10.1007/s00024-018-2014-7.

Onaisi, A., C. Durand, and A. Audibert (1994), Role of hydration state of shales in borehole stability studies, *Soc. Pet. Eng. - Rock Mech. Pet. Eng. 1994*, pp. 275–285.

Paterson, M. S., and T. F. Wong (2005), Experimental Rock Deformation - The Brittle Field, in *Exp. Rock Deform. - Brittle F.*, p. 32, Springer-Verlag, Berlin/Heidelberg, doi:10.1007/b137431.

Payan, C., V. Garnier, J. Moysan, and P. A. Johnson (2009), Determination of third order elastic constants in a complex solid applying coda wave interferometry, *Appl. Phys. Lett.*, doi:10.1063/1.3064129.

Peng, J., and S. Q. Yang (2018), Comparison of mechanical behavior and acoustic emission characteristics of three thermally-damaged rocks, *Energies*, *11*(9), doi:10.3390/en11092350.

Planès, T., E. Larose, V. Rossetto, and L. Margerin (2015), Imaging multiple local changes in heterogeneous media with diffuse waves, *J. Acoust. Soc. Am.*, *137*(2), 660–667, doi:10.1121/1.4906824.

Powell, J. H. (2010), Jurassic sedimentation in the Cleveland Basin: a review, *Proc. Yorksh. Geol. Soc.*, *58*(1), 21–72, doi:10.1144/pygs.58.1.278.

Pye, K. (1985), Electron microscope analysis of zoned dolomite rhombs in the Jet Rock Formation (Lower Toarcian) of the Whitby area, U.K., *Geol. Mag.*, *122*(3), 279–286, doi:10.1017/S0016756800031496.

Ramos da Silva, M., C. Schroeder, and J. C. Verbrugge (2008), Unsaturated rock mechanics applied to a low-porosity shale, *Eng. Geol.*, *97*(1-2), 42–52, doi:10.1016/j.enggeo.2007.12.003.

Renard, F., B. Cordonnier, M. Kobchenko, N. Kandula, J. Weiss, and W. Zhu (2017), Microscale characterization of rupture nucleation unravels precursors to faulting in rocks,

Earth Planet. Sci. Lett., *476*, 69–78, doi:10.1016/j.epsl.2017.08.002.

Renard, F., J. Weiss, J. Mathiesen, Y. Ben-Zion, N. Kandula, and B. Cordonnier (2018), Critical Evolution of Damage Toward System-Size Failure in Crystalline Rock, *J. Geophys. Res. Solid Earth*, *123*(2), 1969–1986, doi:10.1002/2017JB014964.

Rossetto, V., L. Margerin, T. Planès, and E. Larose (2011), Locating a weak change using diffuse waves: Theoretical approach and inversion procedure, *J. Appl. Phys.*, *109*(3), 034,903, doi:10.1063/1.3544503.

Sarout, J., C. Delle Piane, D. Nadri, L. Esteban, and D. N. Dewhurst (2015), A robust experimental determination of Thomsen's δ parameter, *GEOPHYSICS*, *80*(1), A19–A24, doi:10.1190/geo2014-0391.1.

Sarout, J., Y. Le Gonidec, A. Ougier-Simonin, A. Schubnel, Y. Gu??guen, and D. N. Dewhurst (2017), Laboratory micro-seismic signature of shear faulting and fault slip in shale, *Phys. Earth Planet. Inter.*, *264*, 47–62, doi:10.1016/j.pepi.2016.11.005.

Snieder, R. (2002), Coda Wave Interferometry for Estimating Nonlinear Behavior in Seismic Velocity, *Science (80-.).*, *295*(5563), 2253–2255, doi:10.1126/science.1070015.

Sullivan, C., and A. Kaszynski (2019), PyVista: 3D plotting and mesh analysis through a streamlined interface for the Visualization Toolkit (VTK), *J. Open Source Softw.*, *4*(37), 1450, doi:10.21105/joss.01450.

Tarantola, A. (2005), *Inverse Problem Theory and Methods for Model Parameter Estimation*, vol. 120, 1816–24 pp., Society for Industrial and Applied Mathematics, doi:10.1137/1.9780898717921.

Vales, F., D. Nguyen Minh, H. Gharbi, and A. Rejeb (2004), Experimental study of the influence of the degree of saturation on physical and mechanical properties in Tournemire shale (France), *Appl. Clay Sci.*, *26*(1-4 SPEC. ISS.), 197–207, doi:10.1016/j.clay.2003.12.032.

Vomvoris, S., A. Claudel, I. Blechschmidt, and H. Muller (2013), The Swiss Radioactive Waste Management Program - Brief History, Status, and Outlook, *J. Nucl. Fuel Cycle Waste Technol.*, *1*(1), 9–27, doi:10.7733/jnfcwt.2013.1.1.9.

Wang, T., H. Wu, Y. Li, H. Gui, Y. Zhou, M. Chen, X. Xiao, W. Zhou, and X. Zhao (2013), Stability analysis of the slope around flood discharge tunnel under inner water exosmosis at Yangqu hydropower station, *Comput. Geotech.*, *51*, 1–11, doi:https://doi.org/10.1016/j.compgeo.2013.01.006.

Weaver, R. L., and O. I. Lobkis (2000), Temperature dependence of diffuse field phase, *Ultrasonics*, doi:10.1016/S0041-624X(99)00047-5.

Xue, Q., E. Larose, and L. Moreau (2019), Locating structural changes in a multiple scattering domain with an irregular shape, *J. Acoust. Soc. Am.*, *146*(1), 595–602, doi: 10.1121/1.5118246.

Yoshida, N., M. Nishi, M. Kitamura, and T. Adachi (1997), Analysis of mudstone deterioration and its effect on tunnel performance, *Int. J. Rock Mech. Min. Sci.*, *34*(3-4), 353.e1–353.e19, doi:10.1016/S1365-1609(97)00289-X.

Zhang, Y., O. Abraham, F. Grondin, A. Loukili, V. Tournat, A. L. Duff, B. Lascoup, and O. Durand (2012), Study of stress-induced velocity variation in concrete under direct tensile force and monitoring of the damage level by using thermally-compensated Coda Wave Interferometry, *Ultrasonics*, *52*(8), 1038–1045, doi:10.1016/j.ultras.2012.08.011.

Zhang, Y., T. Planès, E. Larose, A. Obermann, C. Rospars, and G. Moreau (2016), Diffuse ultrasound monitoring of stress and damage development on a 15-ton concrete beam, *J. Acoust. Soc. Am.*, *139*(4), 1691–1701, doi:10.1121/1.4945097.

Zhang, Y., E. Larose, L. Moreau, and G. D'Ozouville (2018), Three-dimensional in-situ imaging of cracks in concrete using diffuse ultrasound, *Struct. Heal. Monit.*, *17*(2), doi: 10.1177/1475921717690938.

Zijp, M., J. Ten Veen, R. Verreussel, J. T. Heege, D. Ventra, and J. Martin (2015), Shale gas formation research: From well logs to outcrop - And back again, *First Break*, *33*(2), 99–106.

Zotz-Wilson, R. (2019), Coda-Analysis: First release of Coda-Analysis, doi: 10.5281/zenodo.3255940.

Zotz-Wilson, R., T. Boerrigter, and A. Barnhoorn (2019), Coda-wave monitoring of continuously evolving material properties and the precursory detection of yielding, *J. Acoust. Soc. Am.*, *145*(2), 1060–1068, doi:10.1121/1.5091012.

Zotz-Wilson, R., Douma, L. A. N. R., J. Dautriat, J. Sarout, D. N. Dewhurst, and A. Barnhoorn (2019), CAcoustic, mechanical, and microstructure data used in: Ultrasonic Imaging of the Onset and Growth of Fractures within Partially Saturated Whitby Mudstone using Coda-Wave Decorrelation Inversion, *4TU Centre for Research Data*, doi: 10.4121/uuid:dc3627dd-8434-4fa3-a4f0-b886c31c1ce2.

Figure 1.

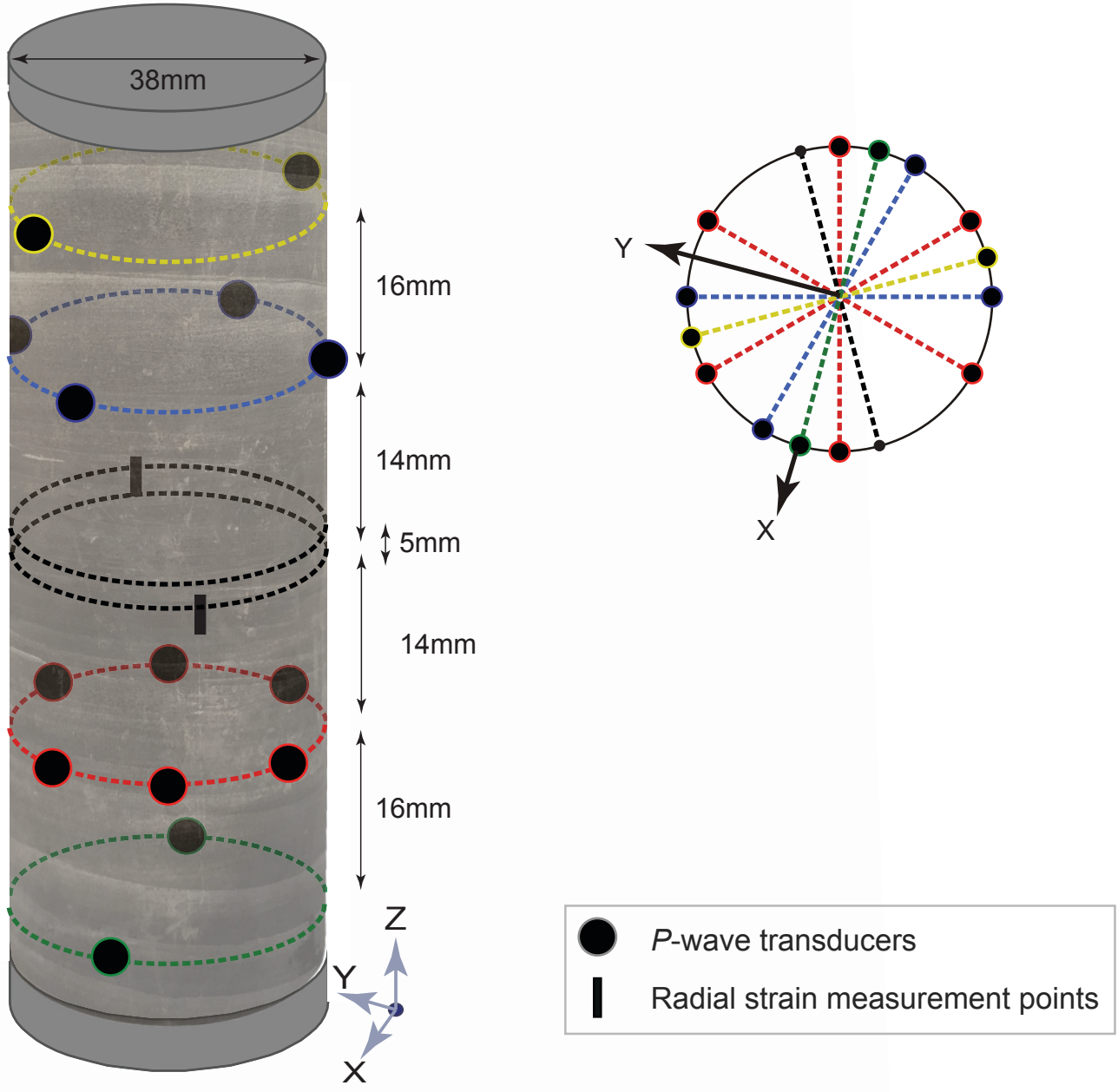
38mm
16mm
14mm
5mm
14mm
16mm
Z
Y
X
Y
X
P-wave transducers
Radial strain measurement points

Figure 2.

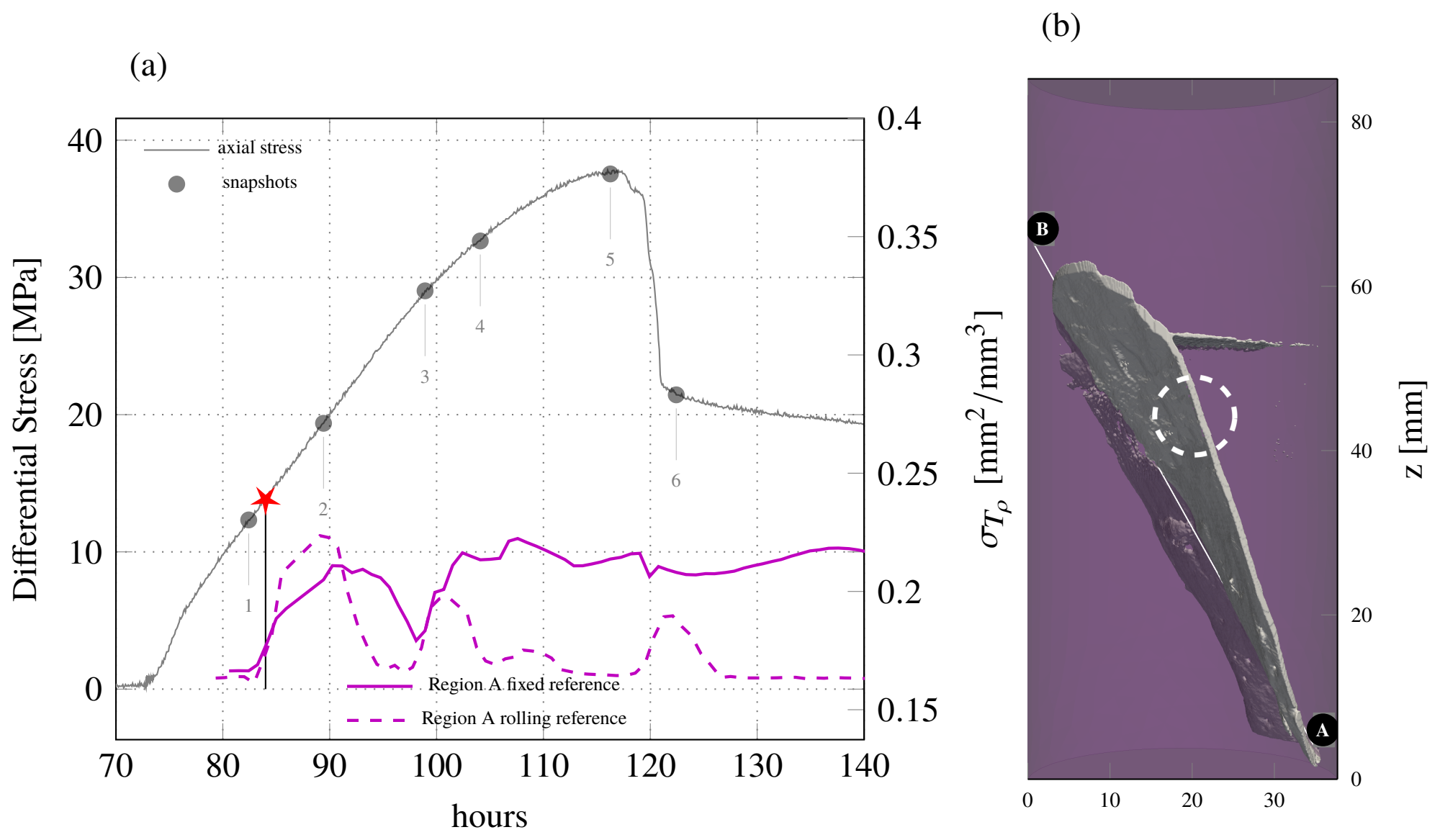
(a)
(b)
axial stress
snapshots
Differential Stress [MPa]
hours
Region A fixed reference
Region A rolling reference
1
2
3
4
5
6
σT_ρ [mm^2/mm^3]
z [mm]
A
B

Figure 3.

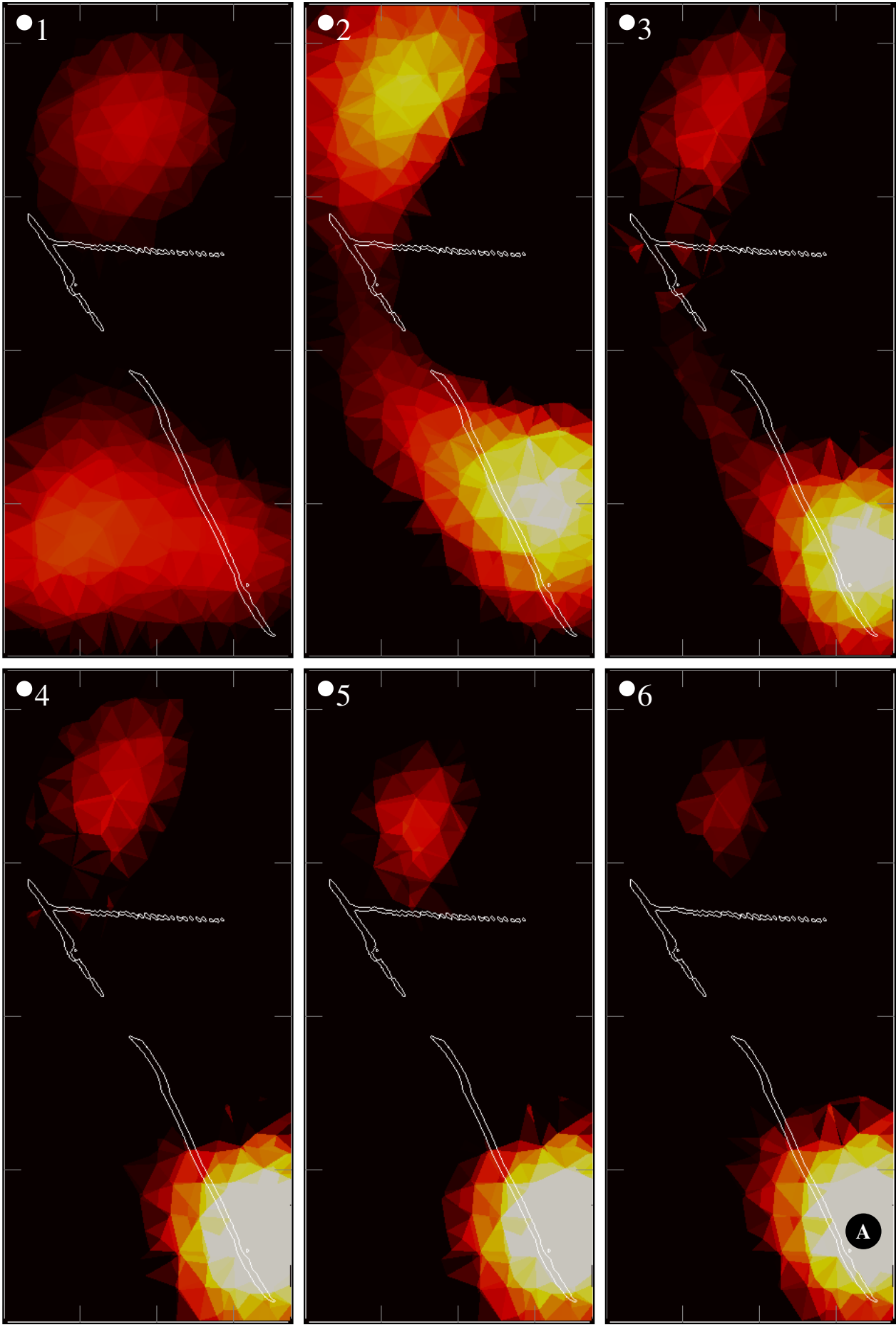
1
2
3
4
5
6
A
0.09
$\sigma_{T\rho}$
0.26

Figure 4.

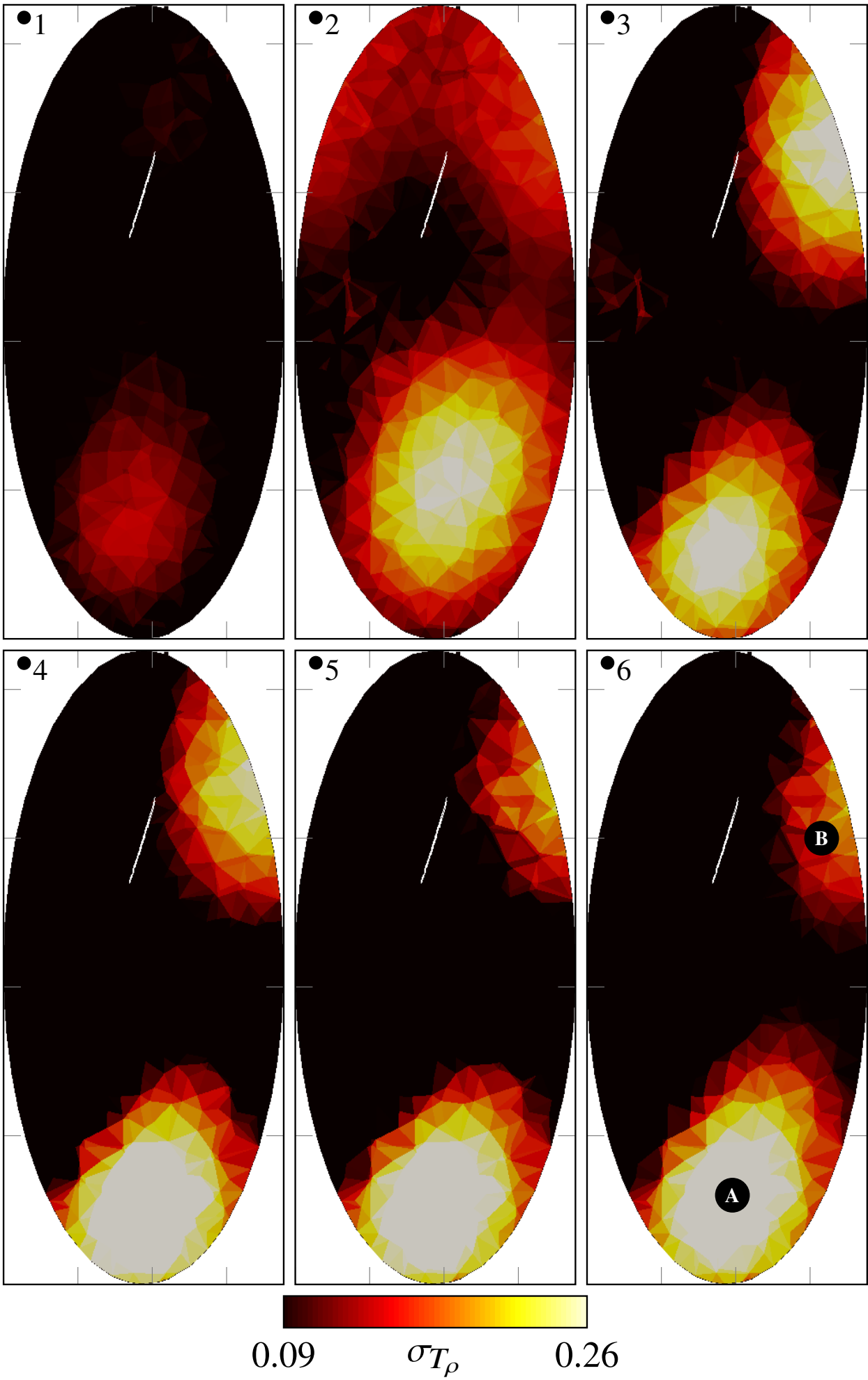
1
2
3
4
5
6
B
A
0.09
σ_{T_ρ}
0.26

Figure 5.

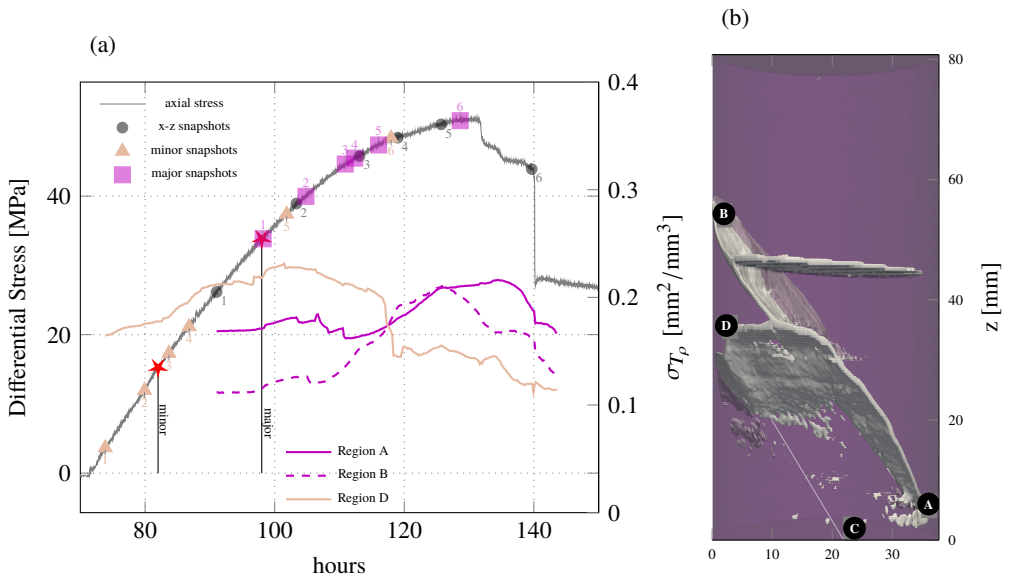
(a)
axial stress
x-z snapshots
minor snapshots
major snapshots
Differential Stress [MPa]
hours
minor
major
Region A
Region B
Region D
(b)
σ_{I_ρ} [mm^2/mm^3]
z [mm]
A
B
C
D

Figure 6.

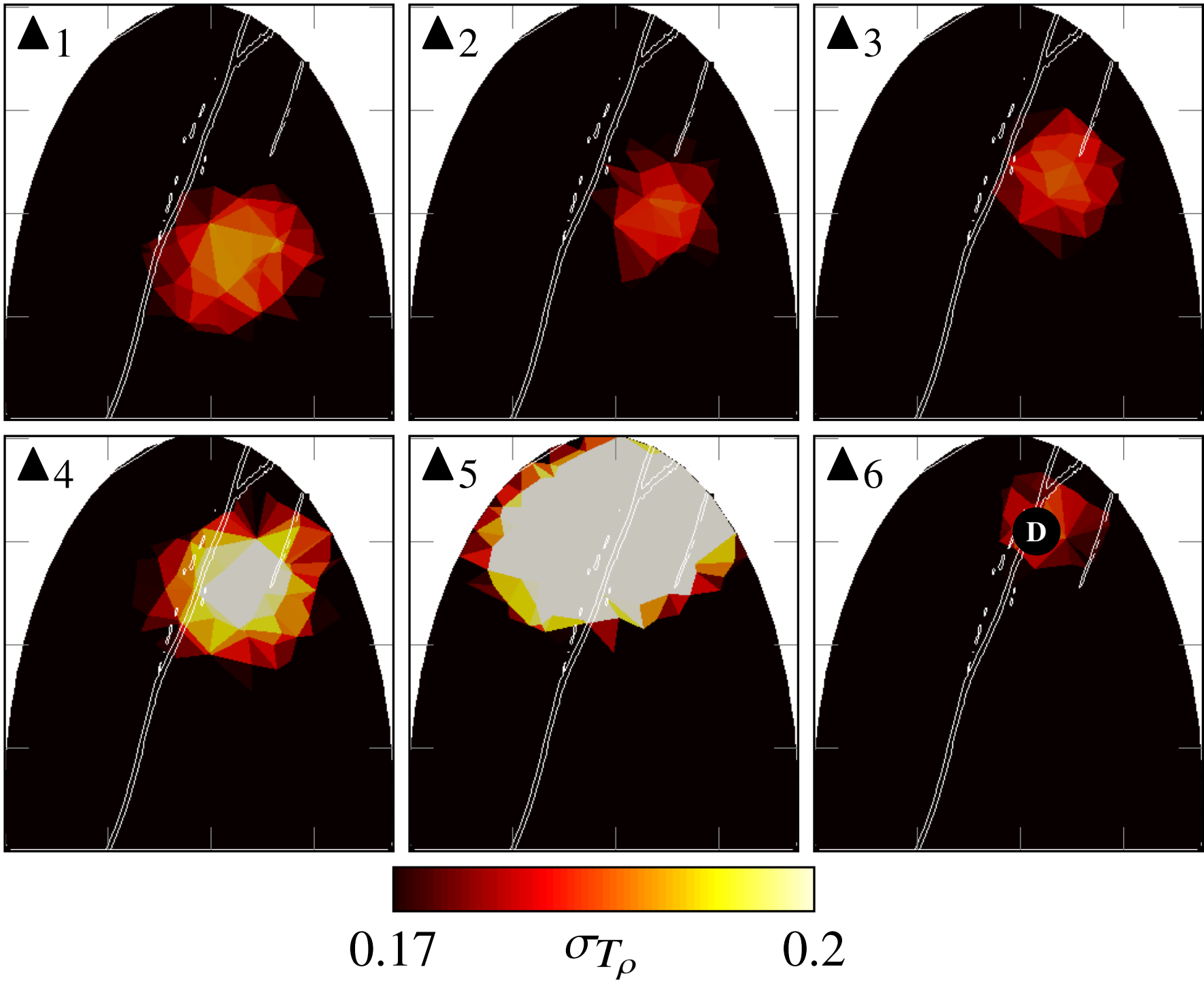
1
2
3
4
5
6
D
0.17
σ_{T_ρ}
0.2

Figure 7.

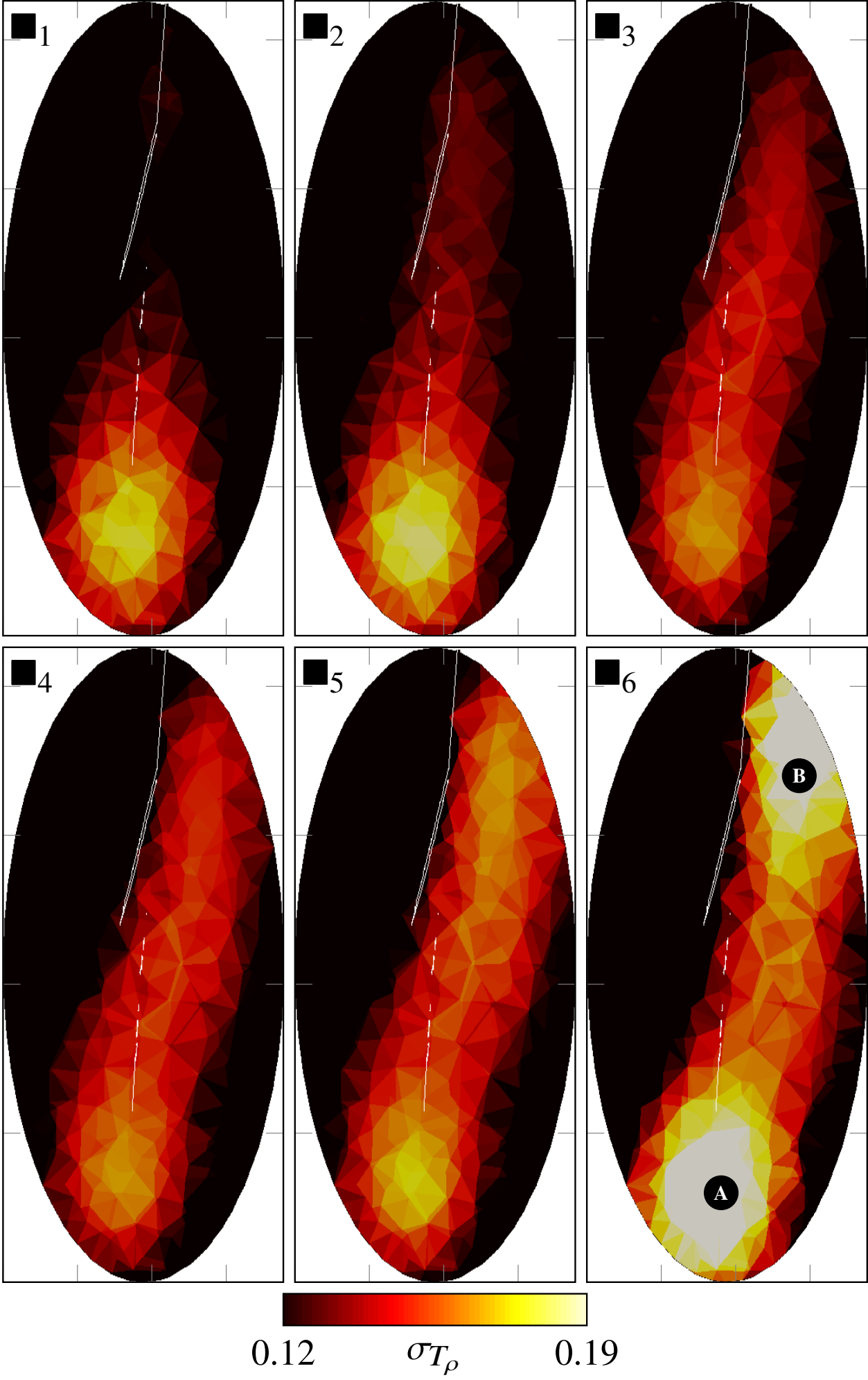
1
2
3
4
5
6
B
A
0.12
σ_{T_ρ}
0.19

Figure 8.

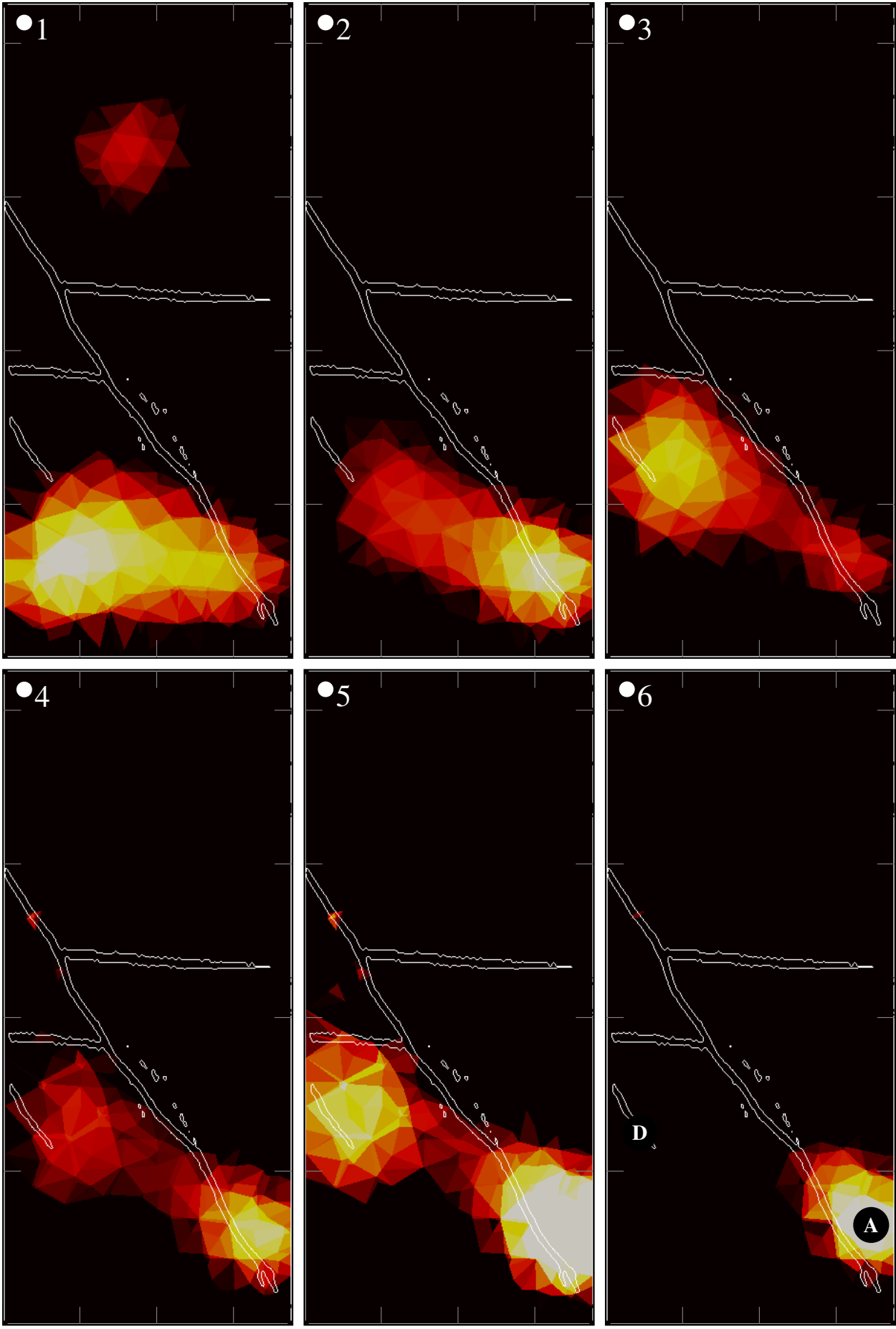
1
2
3
4
5
6
D
A
0.12
σ_{T_ρ}
0.19

Figure 9.

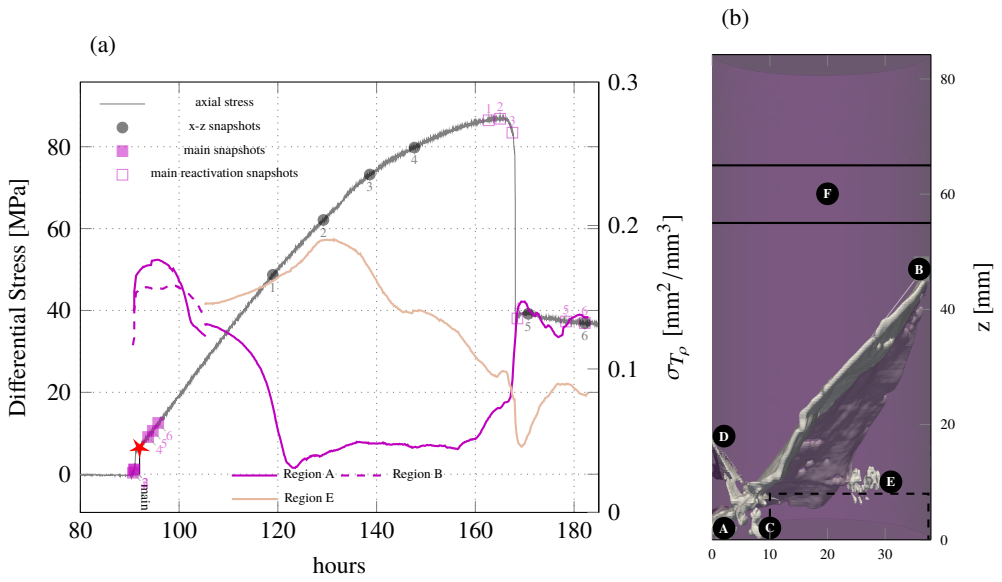
(a)
axial stress
x-z snapshots
main snapshots
main reactivation snapshots
Differential Stress [MPa]
hours
Region A
Region B
Region E
main
(b)
F
B
D
E
A
C
z [mm]
σ_{T_ρ} [mm^2/mm^3]

Figure 10.

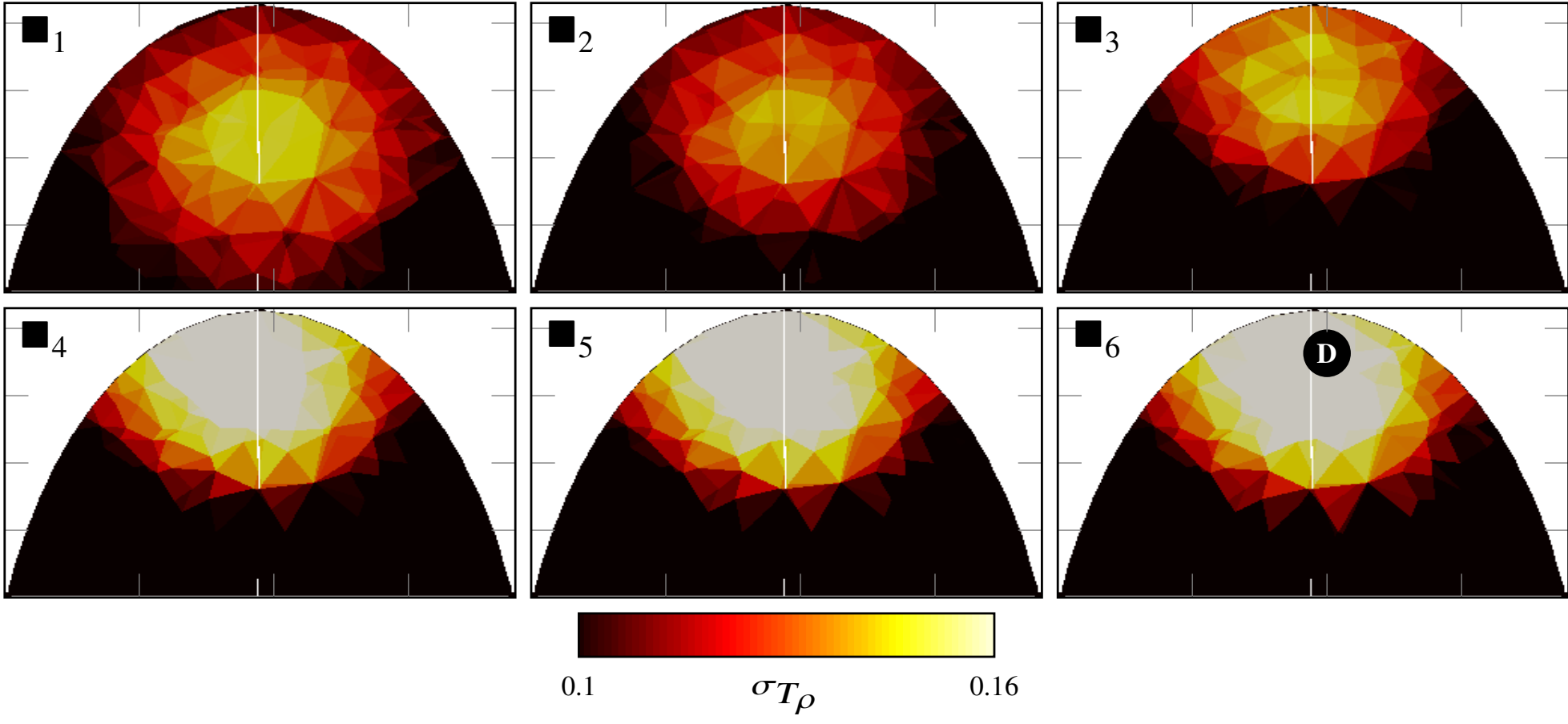
1
2
3
4
5
6
D
0.1
σ_{T_ρ}
0.16

Figure 11.

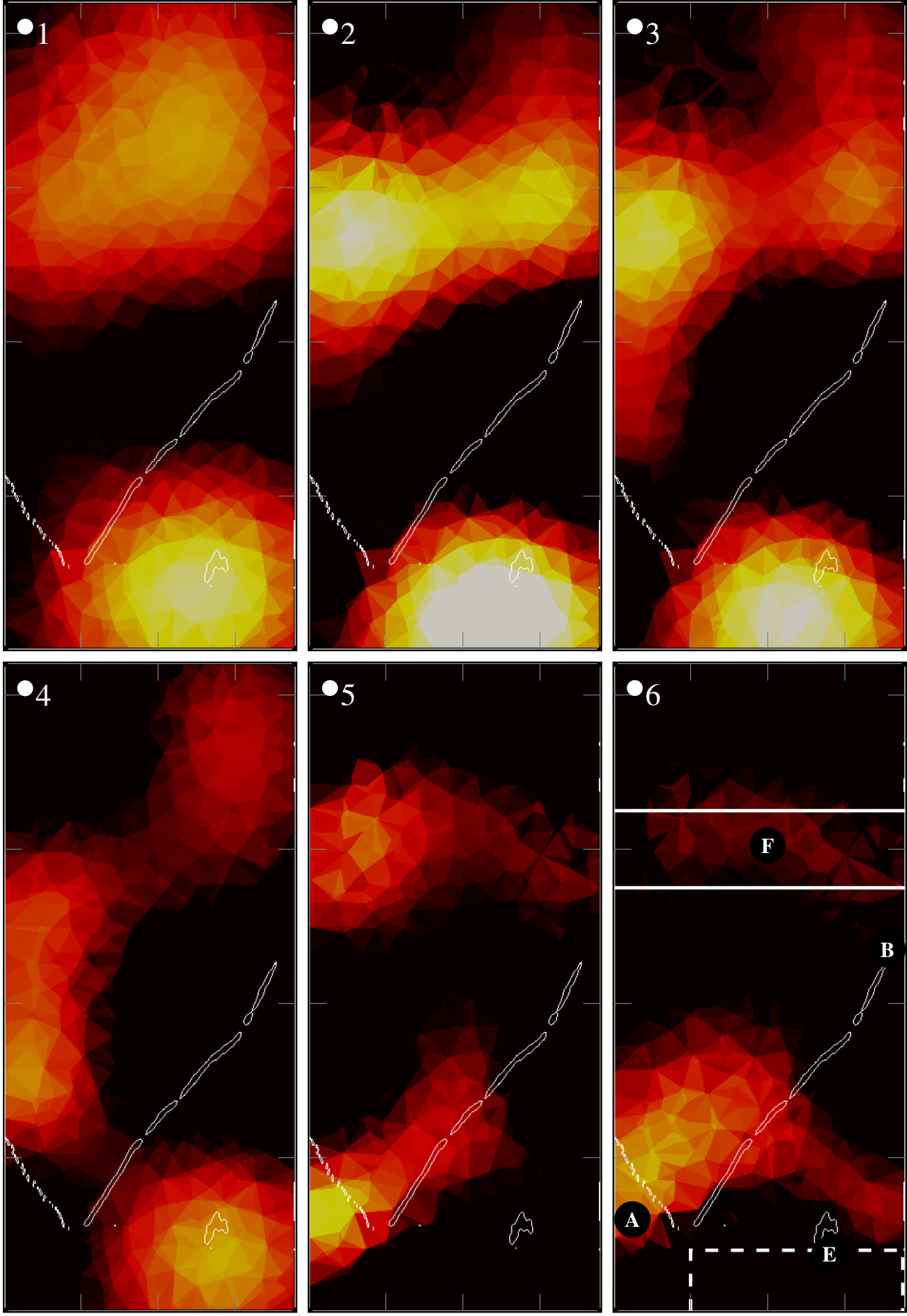
1
2
3
4
5
6
F
B
A
E
0.08
σ_{T_ρ}
0.17

Figure 12.

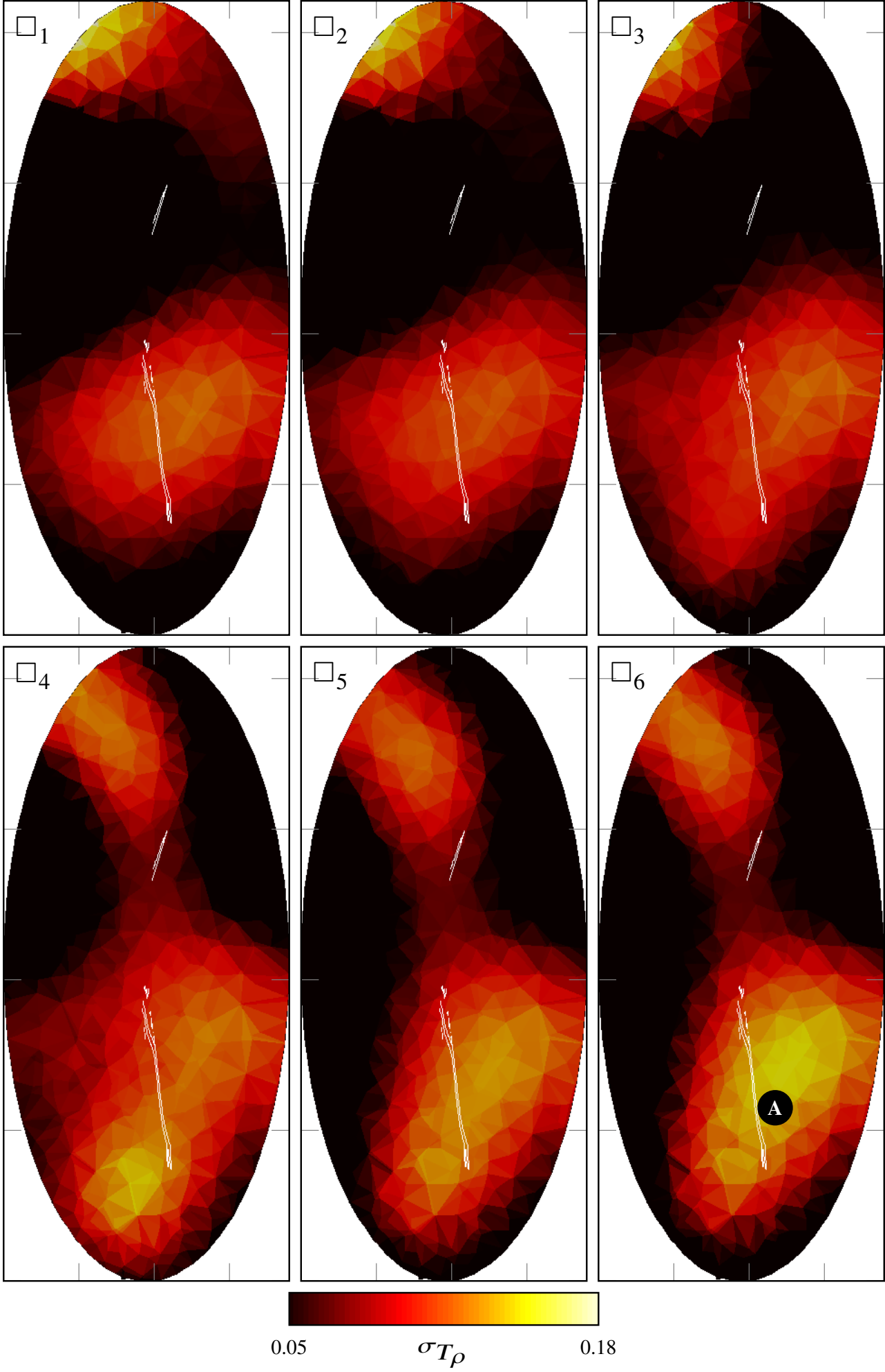
1
2
3
4
5
6
A
0.05
σ_{T_ρ}
0.18

Figure 13.

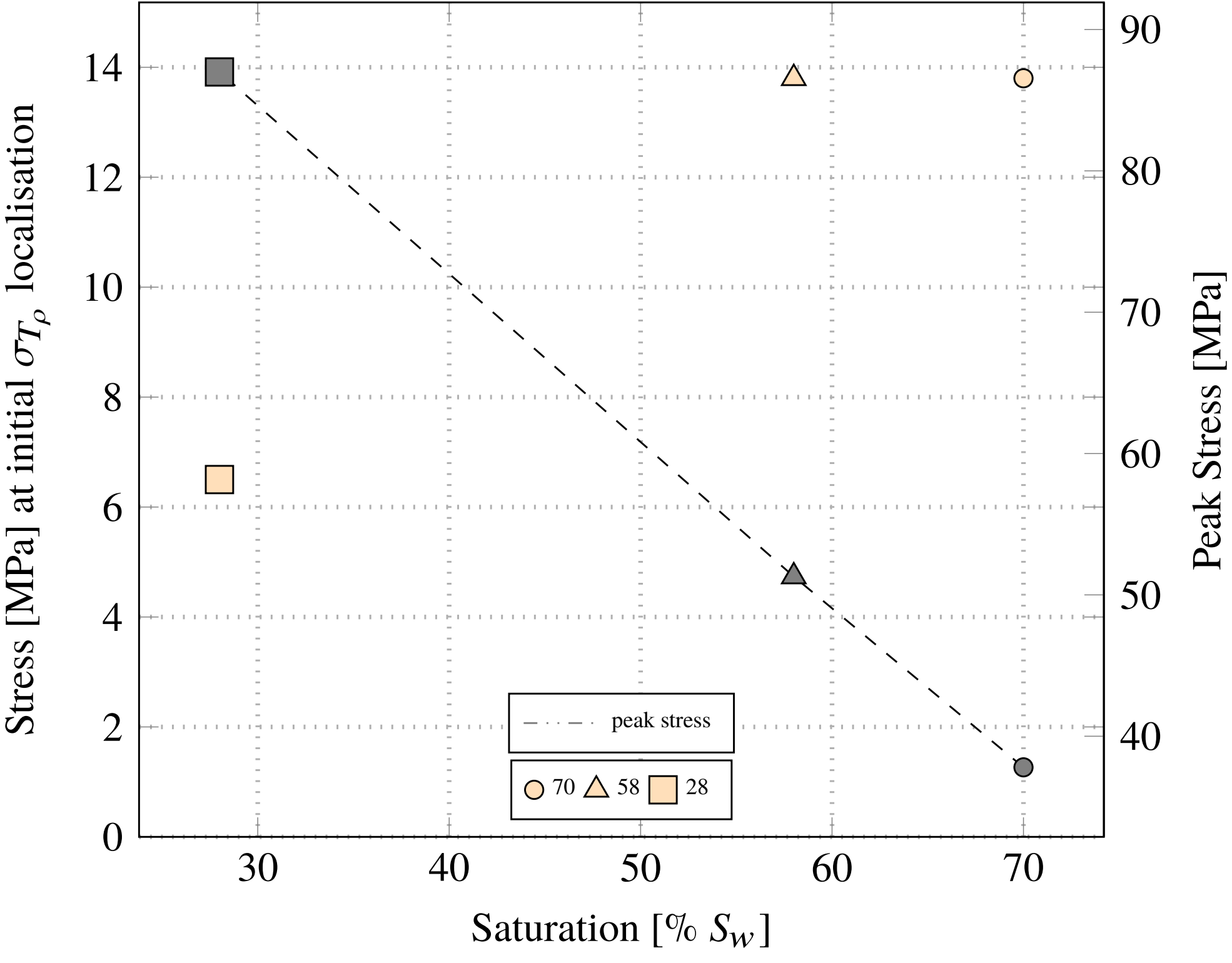
Stress [MPa] at initial σ_{T_ρ} localisation
Peak Stress [MPa]
Saturation [% S_w]
0
2
4
6
8
10
12
14
40
50
60
70
80
90
30
peak stress
70
58
28

Figure 14.

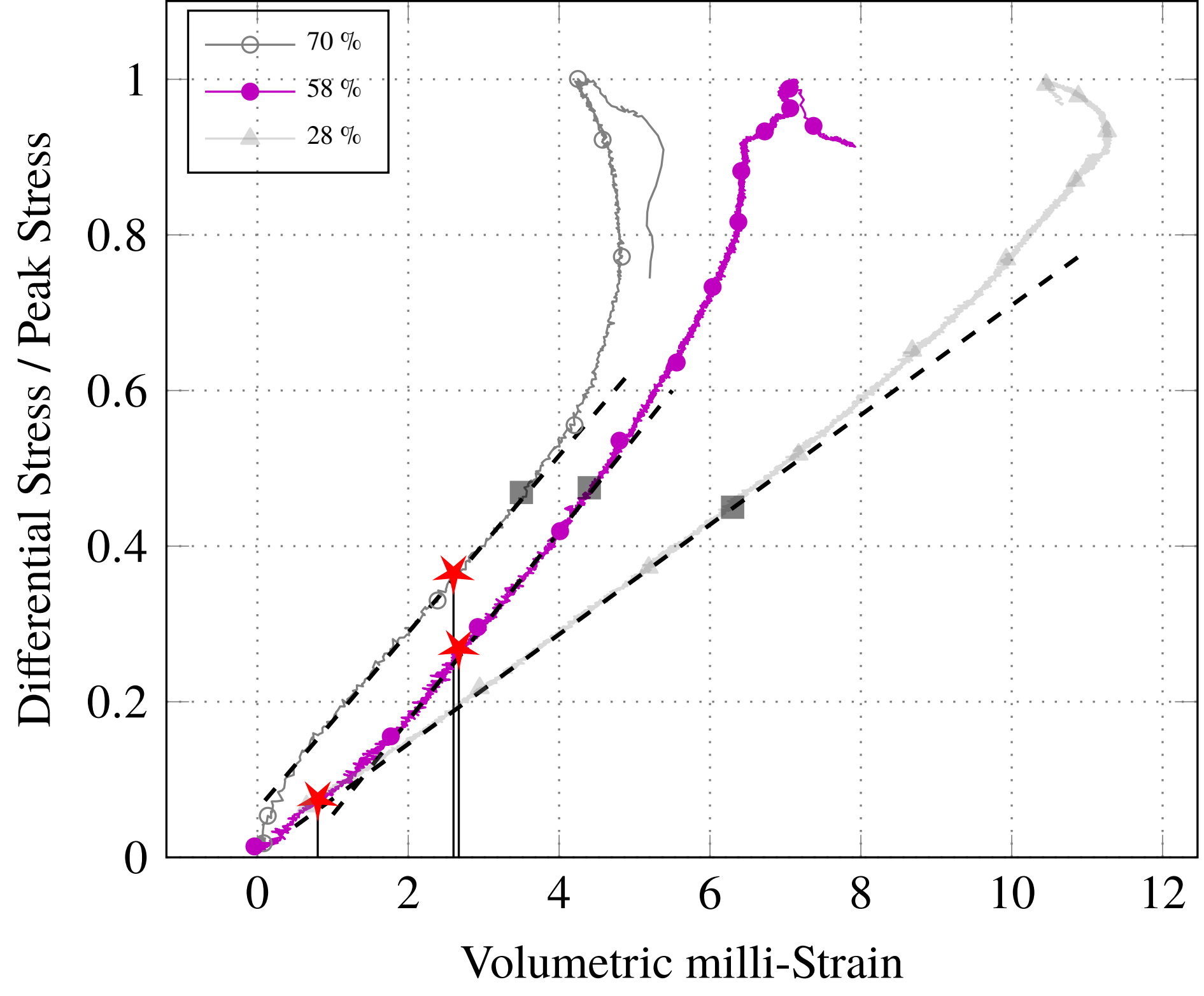
70 %
58 %
28 %
Differential Stress / Peak Stress
0
0.2
0.4
0.6
0.8
1
0
2
4
6
8
10
12
Volumetric milli-Strain